ELSEVIER

Contents lists available at ScienceDirect

Journal of Hazardous Materials

journal homepage: www.elsevier.com/locate/jhazmat





Evaluation of the impact of transition from porous to fractured rock media on 3D field-scale DNAPLs contamination

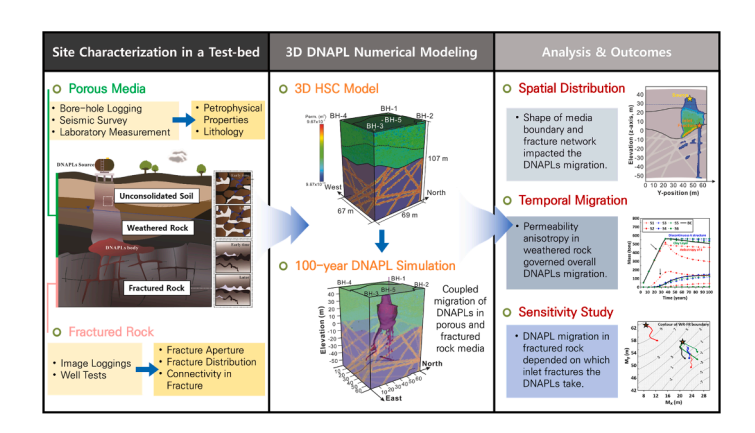
Taehoon Kim^a, Weon Shik Han^{a,*}, Seonkyoo Yoon^b, Peter K. Kang^{b,c}, Jehyun Shin^d, Myung Jin Nam^{e,f}

- ^a Department of Earth System Sciences, Yonsei University, Seoul, Republic of Korea
- ^b Department of Earth and Environmental Sciences, University of Minnesota, Minneapolis, MN, USA
- ² Saint Anthony Falls Laboratory, University of Minnesota, Minneapolis, MN, USA
- ^d Groundwater Environment Research Center, Korea Institute of Geoscience and Mineral Resources, Daejeon, Republic of Korea
- e Department of Energy Resources and Geosystems Engineering, Sejong University, Seoul, Republic of Korea
- f Department of Energy and Mineral Resources Engineering, Sejong University, Seoul, Republic of Korea

HIGHLIGHTS

- Coupled DNAPLs migration in porous and fractured rock media is captured.
- Significant effects of weathered rock fractured rock transition are explored.
- Shape of media boundaries and fracture network impact local DNAPLs migration.
- Permeability anisotropy in weathered rock governs overall DNAPLs contamination.
- DNAPLs fate in fractured rock depends on which inlet fractures the DNAPLs take.

GRAPHICAL ABSTRACT



ARTICLE INFO

Editor: Lingxin Chen

Keywords:
Field Scale DNAPLs Contamination
3D Numerical Modeling
Weathered Rock
Fractured Rock
Site Characterization

ABSTRACT

A 3D high-resolution subsurface characteristic (HSC) numerical model to assess migration and distribution of subsurface DNAPLs was developed. Diverse field data, including lithologic, hydrogeologic, petrophysical, and fracture information from both in situ observations and laboratory experiments were utilized for realistic model representation. For the first time, the model integrates hydrogeologic characteristics of both porous (unconsolidated soil (US) and weathered rock (WR)) and fractured rock (FR) media distinctly affecting DNAPLs migration. This allowed for capturing DNAPLs behavior within US, WR, and FR as well as at the boundary between the media, simultaneously. In the 3D HSC model, hypothetical 100-year DNAPLs contamination was simulated, quantitatively analyzing its spatiotemporal distributions by momentum analyses. Twelve sensitivity scenarios examined the impact of WR and FR characteristics on DNAPLs migration, delineating significant roles of WR. DNAPLs primarily resided in WR due to low permeability and limited penetration into FR through sparse inlet

E-mail address: hanw@yonsei.ac.kr (W.S. Han).

 $^{^{\}ast}$ Corresponding author.

fractures. The permeability anisotropy in WR was most influential to determine the DNAPLs fate, surpassing the impacts of FR characteristics, including rock matrix permeability, fracture aperture size, and fracture + rock mean porosity. This study first attempted to apply the field-data-based multiple geological media concept in the DNAPLs prediction model. Consequently, the field-scale effects of WR and media transitions, which have been often overlooked in evaluating DNAPLs contamination, were underscored.

1. Introduction

Dense Non-Aqueous Phase Liquids (DNAPLs) contamination has been a persistent conundrum worldwide since the late 20th century, drawing significant concern due to its hazardous effect on soil, groundwater resources, and, eventually, human health [14,22,36,40]. The potential threats of DNAPLs contamination are pervasive, due to its diverse applications, encompassing manufacturing industries (e.g. metal cleaner, degreaser, and paint stripper) household products (e.g. spot remover and finishes), and agriculture (e.g. pesticide and herbicide) [7, 29]. Widely encountered DNAPLs include hundreds of chemical compounds, such as trichloroethylene (TCE, C2HCl3) tetrachloroethylene (PCE, C2Cl4), carbon tetrachloride (CT, CCl4), and polychlorinated biphenyls (PCBs), that are listed as priority contaminants by US EPA and well-documented for their chemical structures and toxicity [10,2,25, 34]. In addition to their toxicity, leaked DNAPLs in the subsurface are devastating due to their unpredictable distribution and challenging remediation. With their low solubility in water (< 2%) and higher density than water, DNAPLs migrate extensively below the groundwater table, contaminating multiple aquifers and geological media. As the DNAPLs penetrate deeper, they encounter transition of biochemical (e.g. redox and aerobic/anaerobic conditions, and microbes activity) and geophysical (e.g. pressure, temperature, particle size distribution, capillarity, and geologic media types) conditions [1,22,26,3,4].

The transition of geological media is one crucial consideration for the subsurface DNAPLs migration. The downgoing DNAPLs migrate through both porous media (e.g. unconsolidated soil, weathered soil, and weathered rock) and underlain fractured rock media. Within porous media, DNAPLs migrate through pore spaces primarily driven by gravitational force and pressure gradient, largely influenced by media properties such as capillary pressure, sorption capability, and geostructural heterogeneity [31,34,60]. Once reaching the fractured rock media, however, DNAPLs migrate through networks of high permeable fractures, facilitating their preferential transport over significant distances [9,34]. For decades, extensive studies have addressed the distinct DNAPLs flow and solute transport processes in each media via both experimental and numerical investigations [13,15,19,23,41,45,5,51, 56]. Nevertheless, their experimental or numerical model domains were constrained to either porous or fractured rock media individually, without considering the hydrodynamical transition that occurred at the boundary between the media. Additionally, the studies were primarily based on pore-, laboratory- to pilot-scale observations and conducted under a simplified and controlled setup. For example, some of the studies assumed planar boundaries between different geologic materials [17,64]. These approaches may not be sufficient to fully capture the influence of heterogeneous and irregular stratification, geostructures, or hydrologic properties in practical contaminated sites [27,28].

At the site- or field-scale, the transition from porous media to fractured rock media becomes much more complicated due to the influence of weathering and erosional processes, which impart structural complexity and hydrogeological heterogeneity adjacent to the transition boundary. This boundary often becomes non-planar, due to the irregularities in the erosion and weathering, driven by local properties variation [42,54]. The gradual shift from coarse to fine grains resulting from the weathering process leads to hydraulic discontinuity and multi-directional disturbance in fluid flow and solute transport [33,35,55]. Recent investigations have emphasized the crucial roles of weathered media in the DNAPLs migration. [28] reported the impact of

partially-weathered and fully-weathered rock layers on lateral and vertical hydraulic conductivity variation during TCE remediation. [32] delineated the significant differences in TCE transport and fate according to the presence of a weathered zone on the fractured rock. Despite the recent recognition of the significance of weathered media, to the best of our knowledge, no previous studies have quantitatively assessed the field-scale implications of the transition from porous to fractured rock media when influenced by weathered media, in the context of DNAPLs contamination.

In this study, a novel approach by way of developing a comprehensive field-scale 3-dimensional (3D) numerical model that integrates both porous media (unconsolidated soil, weathered rock) and fractured rock media was presented to evaluate the 3D DNAPLs migration and distribution. In the model, the characteristics of both media and their configuration of the transition boundary were implemented. Realistic and high-resolution hydrogeologic and geostructural characteristics are integrated into the 3D model using data obtained from various field investigation techniques, including seismic surveys, geophysical logging, and hydraulic well tests. The study evaluated hypothetic DNAPLs migration and distribution under varying geostructural properties of the weathered rock and hydrogeologic properties in the fractured rock through a rigorous momentum analysis. Notably, the analysis highlighted the significant influence of weathered rock properties on the subsurface behavior of DNAPLs, which often exhibit substantial uncertainties and have been overlooked in previous research.

2. Characterization of Deokso test-bed

The Smart Subsurface Environment Management (SmartSEM) Korean research center designed the field investigation at Deokso testbed located in Gyeong-gi province, approximately 20 km east of Seoul, South Korea (Fig. 1). The test-bed is not an actual contaminated site, instead the primary objective of the project was to construct a 3D high-resolution subsurface characterization (HSC) model. The model incorporated unconsolidated soil, weathered rock, and fractured media to the depth of approximately 100 m, where various field techniques of geophysical survey, borehole-logging, well tests, and groundwater monitoring were implemented (Table S1). The constructed 3D HSC model was applied to elucidate the migration behavior of dense non-aqueous phase liquids (DNAPLs) in multiple geological media.

2.1. Lithologic information through 5 drilled boreholes

The size of Deokso test-bed was 67 m \times 69 m where 4 characterization wells (BH-1, BH-2, BH-3, and BH-4) were drilled at the corner, and BH-5 was drilled at the center (Fig. 1). The drilled depths of BH-1, BH-2, BH-3, BH-4, and BH-5 were 100.6 m, 87 m, 100.6 m, 103.0 m, and 100.6 m from the ground surface, respectively (Fig. 2). To hold up the drilled boreholes and to prevent the collapse of unconsolidated soil, casings were installed to the depth of 49.4 m, 45 m, 41.8, 42 m, and 24 m for BH-1, BH-2, BH-3, BH-4, and BH-5, respectively (Fig. 2a). The analyses of drilled cores aid to characterize high-resolution lithologic information including the bounding depth between porous media and fractured rock. The zone of porous media consists of unconsolidated soil (US: buried layer, colluvium, sedimentary soil, and weathered soil) and weathered rock (WR). Below, the zone of fractured rock (FR) includes layers of both soft and hard rock. The boundaries between porous media (US and WR) and FR are located at 34 m, 42 m, 36.5 m, 42.5 m, and

62.5 m depths of BH-1, BH-2, BH-3, BH-4, and BH-5, respectively (the boundaries between the red-colored WR and gray-colored soft rock in Fig. 2b). Thus, the WR distributes to the deepest depth at the center (BH-5) and becomes shallow toward the edge of the test-bed (BH-1, BH-2, BH-3, and BH-4), forming a bowl-shaped boundary between US+WR and FR.

The depths of the groundwater table at BH-1, BH-2, BH-3, BH-4, and BH-5 were varied at 22.30 m, 21.87 m, 19.80 m, 21.80 m, 22.12 m, respectively (Fig. 2c). Overall, groundwater flows from east (BH-2 and BH-3) to west (BH-1 and BH-4), despite slightly high groundwater level at the BH-5.

2.2. Lithologic information through sonic log, gamma-ray log, and seismic survey

The lithologic information characterized by the drilled-core analysis was cross-checked with geophysical logging and survey techniques, such as sonic logs, gamma-ray logs, and 2D cross-sectional inversion data obtained from surface refraction seismic surveys [63] (Table S1).

The sonic logs were acquired from the 5 boreholes (BH-1, BH-2, BH-3, BH-4, and BH-5). During the sonic logging, the probe vertically recorded the P-wave velocity from the sonic wave, that propagates through the surrounding matrix. Since the P-wave velocity implicates the hardness of the surrounding matrix, the boundaries between weathered rock, soft rock, and hard rock were identified by detecting discontinuity (dramatic change) in the continuous P-wave velocity log (Fig. S1a). As a result, the depth of discontinuity in P-wave velocity was relatively deeper at BH-2, BH-3, and BH-5 (eastern part of the test-bed) than at BH-1 and BH-4 (western part). The natural gamma-ray loggings detected the gamma-ray radiated from natural K, U, and Th. The average intensity of the natural gamma-ray from 5 boreholes was 137 API [50]; the intensities of US, WR, and FR were the smallest, intermediate, and largest, respectively (Fig. S1b). Spatially, the average intensity of gamma-ray at BH-1 and BH-4 was higher than at BH-2, BH-3, and BH-5; the intensities over 500 API appeared only at BH-1 and BH-4, due to the presence of high-radiative intrusive rocks or dikes. Additionally, the spectral gamma-ray log that predicts concentrations of K, U, and Th was implemented to investigate the potential geological connectivity between the boreholes (Fig. S1c). In sum, the patterns of sonic, natrual and spectral gamma ray logs indicated non-planar and irregular structure of lithologic boundary in the test-bed.

At the ground surface, a series of refraction seismic surveys were conducted. The refraction survey using a 3.6 kg (8 lb) sledgehammer as a seismic source and 12 geophones as a receiver was implemented along the 55 m survey line (H-1) crossing BH-2 and BH-4 to the NE direction (Fig. S2a). Two additional surveys along 115 m survey lines (SRD-1 and

SRD-2) employing the dynamite blast were implemented to explore the depth of FR. The mapping results of the surface seismic survey were supported by additional well-to-well and surface-well seismic surveys [63]. The results showed that the fractured rock boundary was bowl-shaped toward the BH-2 from the BH-4, similar to the interpretation from sonic and gamma-ray logs.

2.3. Petrophysical properties through neutron logging and laboratory measurements

The neutron porosity distribution at 5 boreholes was measured by neutron intensity loggings (Fig. 2a). A single neutron probe with a diameter of 41.3 mm was utilized, due to constraints for the 50 mm inner-diameter steel casings. After obtaining thermal neutron count rates (ψ) in the boreholes, the logging datasets were converted to water-filled porosities (neutron porosity, ϕ). The conversion between ψ and ϕ was computed with an empirical relationship (Fig. S3a); the empirical relationship was established through a calibration test using a known single neutron count rate vs. neutron porosity data obtained from reference granite, water, and limestone test blocks located at the radioactivity calibration facility in Pohang center of Korea Institute of Geosciences and Mineral Resources (Fig. S3b). The empirical equation calculating ϕ with respect to ψ is as follows:

$$\phi = 79.87 - 1.62682 \times 10^9 (1 - e^{-\frac{\psi}{1.9699 \times 10^{11}}}) - 67.2(1 - e^{-\frac{\psi}{117.556}})$$
[1]

The obtained neutron porosity data were then compared with laboratory measurements by mercury injection porosimeter (MIP). For the comparison, 7 core samples from BH-3 were used; each sample was collected from the depth of US (N-1 and N-2), WR (N-3 and N-4), and FR (N-5, N-6, and N-7), respectively (Fig. 2a). Overall, the neutron porosity data were matched well with the laboratory measured MIP data. Below the depth of groundwater table where neutron loggings were able to implement, the neutron porosity data properly approximate the laboratory MIP porosities where the values for the sample N-3 (20.8 m), N-4 (27.2 m), N-5 (37.1 m), N-6 (66.0 m), and N-7 (73.6 m) were 20.06%, 13.74%, 4.03%, 5.30%, and 0.22%, respectively. For N-1 (9.0 m) and N-2 (10.1 m) above the groundwater table, the MIP measurement resulted in 44.97% and 41.86%, respectively. Markedly, the validated neutron porosity in porous media (US+WR) where the average porosity at each borehole (BH-1: 34.79%, BH-2: 18.74%, BH-3: 16.13%, BH-4: 19.30%, and BH-5: 11.98%) largely decreases in FR (BH-1: 15.32%, BH-2: 9.00%, BH-3: 6.93%, BH-4: 4.84%, and BH-5: 3.59%).

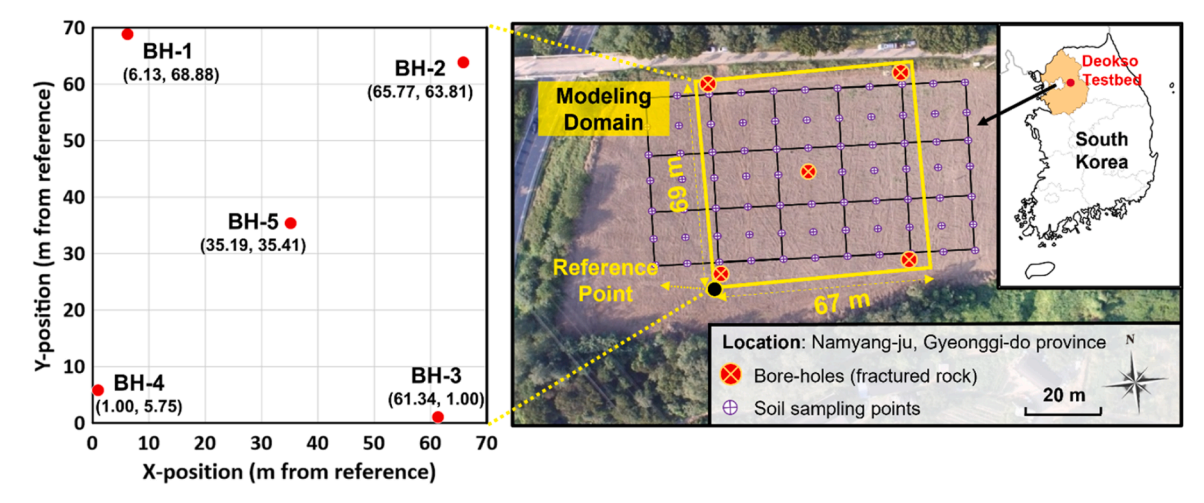


Fig. 1. Description of Deokso test-bed and domain of interest for numerical modeling.

2.4. Fracture properties through image loggings and well tests

Optical televiewer (OTV), temperature, sonic, and caliper loggings, and hydraulic pumping tests were conducted to identify subsurface fracture distribution and also to characterize transmissible fractures (Table S1). The OTV panoramically scanned the borehole perimeters to detect fracture properties including dip angle, azimuth, and aperture size (Fig. S4a). Through analyzing the OTV image loggings, 90, 77, 62, 86, and 58 fractures were detected at boreholes BH-1, BH-2, BH-3, BH-4, and BH-5, respectively. For each of the detected fractures, dip angle, azimuth, and aperture size were measured (Fig. S4b and S4c). The measurement indicates that the major orientation of the fractures was 40–60° SE with the mean (13.03 mm) and median (7.53 mm) of the aperture sizes, respectively. The sonic, caliper, and differential temperature loggings were then implemented to quickly estimate the

location of the transmissible fractures that potentially serve as major pathways of groundwater flow (Fig. S5). The sudden changes in the sonic velocity, borehole diameter, and temperature logs indicate groundwater inflows from fractures or outflow to fractures. For example, the sonic velocity is attenuated while the borehole diameter is increased, indicating the presence of fractures surrounded by weakened and excavated matrix.

After the logging analyses, single and multi-well hydraulic tests were implemented to determine the exact locations of the transmissible fractures. At BH-5, during both single-well pumping and the following recovery stage, temporal changes in groundwater level, groundwater temperature, and electrical conductivity were monitored (Fig. S6). From hydrogeologic responses, two major transmissible fractures respectively dipping toward 32° and 57° SW were identified at 54 m and 57.5 m depth. To investigate the connectivity of these 2-transmissible fractures

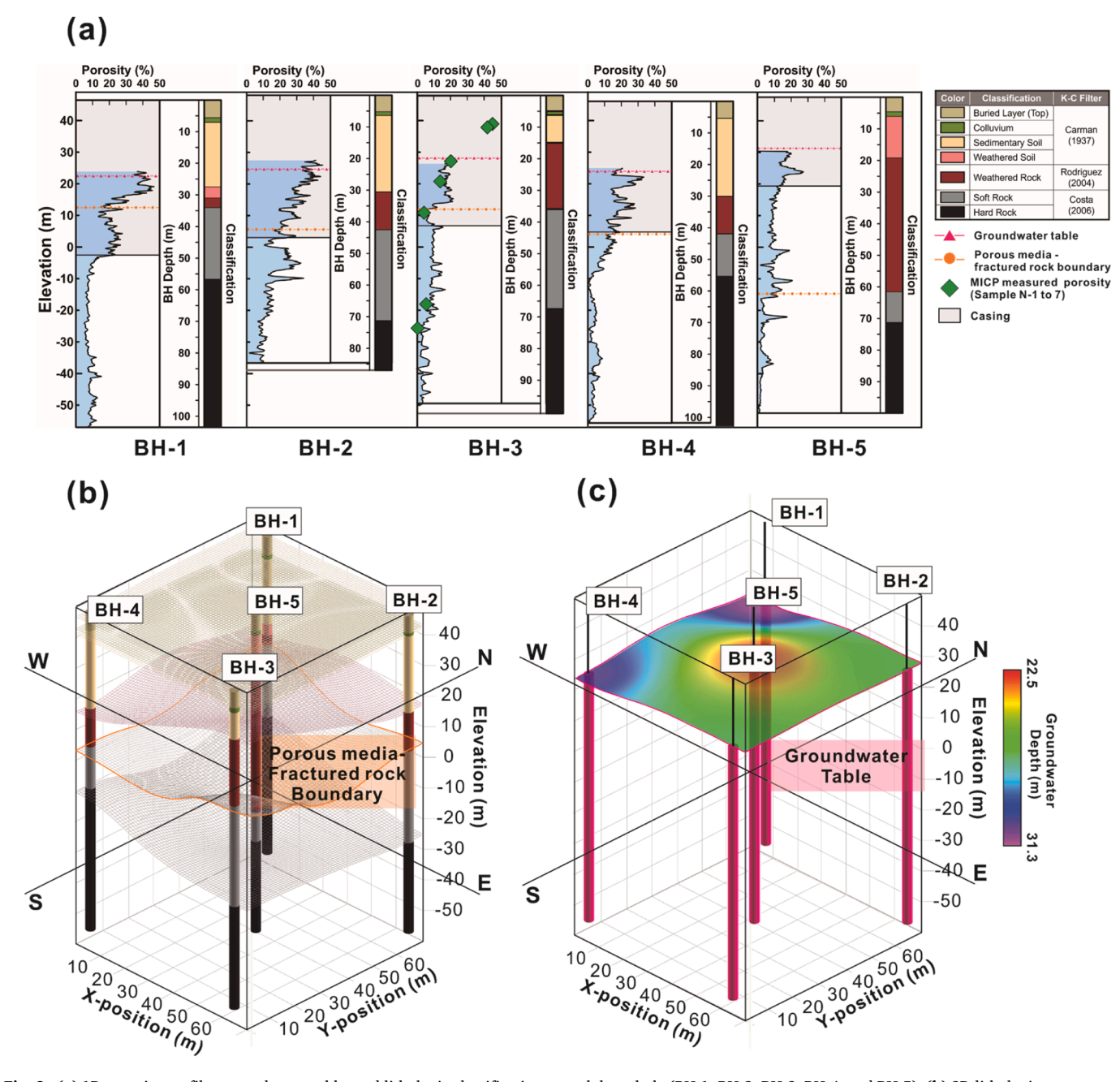


Fig. 2. (a) 1D porosity profile, groundwater table, and lithologic classification at each bore-hole (BH-1, BH-2, BH-3, BH-4, and BH-5). (b) 3D lithologic contacts and the porous-rock media boundary. (c) Data-interpolated 3D groundwater surface.

to BH-1, BH-2, BH-3, and BH-4, additional multi-well tests were performed. After packing in the vicinity of the 2-transmissible fractures in BH-5, groundwater was pumped at a 40 L/min rate for 40 h. Then, hydrogeologic responses were monitored at the other 4 boreholes. Consequently, the groundwater level only dropped at BH-2 and BH-3, confirming hydrogeologic connection through major fractures between BH-2, BH-3, and BH-5. Finally, the locations of the connected fractures at BH-2 and BH-3 were identified by a flowmeter test. The vertical groundwater velocity changes were detected at depths of 55 m and 64 m in BH-2, and a depth of 64 m at BH-3 respectively, indicating the presence of connected fractures. Following similar procedures, a total of 12 major permeable fractures were identified (Table S2) [50].

3. Construction of 3D subsurface characterization model

By integrating field-observed lithologic, geophysical, and hydrogeological datasets, the 3D HSC model was developed (Fig. 3a). The HSC model consists of $67 \times 69 \times 107$ (494,661) uniform cubic ($1 \times 1 \times 1$ m³) grid-blocks covering the Deokso test-bed. The surface elevation ranged from 46.07 to 48.08 with the highest elevation of 49 m and the bottommost elevation was -56 m. The boundary between porous media (US and WR) and fractured rock (FR) varied from -10–15 m.

3.1. Porous media zone (Unconsolidated Soil and Weathered Rock)

In porous media (US and WR), the 3D heterogeneous porosity distribution was reproduced by the sequential indicator simulation (SISim) geostatistic method [43]. Utilizing the field neutron porosity data calibrated by MIP data as hard data, the SISim method generated multiple equiprobable heterogeneous porosity distributions while preserving statistical properties of the field data (Fig. S7). The method preserved the means and variances of neutron porosity data and reflected adequately the discontinuities between porous media and fractured rock. The assigned parameters for the geostatic representation were listed in Table S3.

From the porosity distribution, 3D permeability distributions were determined by implementing Kozeny-Carman (K-C) based porosity-permeability conversion (Fig. 3b). Different conversion equations variable to each of US and WR were applied in each media. For US, considering the soil texture of the Deokso test-bed mainly composed of sandy loam and silty clay loam, the K-C equation developed by [58] was adopted as $k=\frac{\phi^3}{Br^2S^2}$, where ϕ is porosity, B is the coefficient regarding pore shape, τ is the tortuosity, and S is the specific surface area. The values for B (2.0), τ (1.389) and S (2.65 \times 10⁴ m²/g) were determined from [18] and [20]. The K-C equation for WR was the power-law permeability equation as $k=C_c\frac{\phi^m}{1-\phi}$ [16]. Here, a Kozeny-like coefficient (C_c) was 1.46 \times 10⁻¹³, and empirical tortuosity factor (m) varing within 1 < m < 4 was assigned to 1.47. The K-C conversion-based

permeabilities were verified through laboratory gas permeability tests (Table S1). The experimental permeabilities measured from the three WR core samples (N-3: 20.8 m, N-4: 27.2 m, and N-5: 37.0 m) at BH-3 were 2.25×10^{-14} m², 1.57×10^{-15} m², and 3.16×10^{-15} m², respectively. The K-C conversion permeabilities at corresponding depths were 2.63×10^{-14} m², 3.95×10^{-15} , and 9.55×10^{-15} m², respectively, showing small differences within an order of magnitude (Fig. 3b).

3.2. Fractured rock zone

In fractured rock media (FR), the 3D fracture network distribution can be generated by employing both stochastic and deterministic approaches. The statistical information of the fracture network obtained by the OTV logs (Fig. S4b and S4c) enables stochastic generation of equiprobable realizations of discrete fracture network (DFN). On the other hand, the 12 major permeable fractures identified by both pumping tests and OTV logs enable the generation of deterministic DFNs. In this study, the information of the 12 deterministic fractures was used for the DFN generation due to the dominant role of major permeable fractures as primary pathways of DNAPLs migration at the field scale (Table S2). The generated 3D DFN was subsequently upscaled to a continuumequivalent permeability distribution, as the DFN can not be directly interchanged with the continuum representation of upper porous media [47]. An upscaling algorithm known as upscaled discrete fracture matrix model (UDFM) was adopted [53]. Details of the methodology are referred to [53] while a brief description of the algorithm is summarized here. The UDFM generates unstructured tetrahedra meshes which are flexible to generate fine meshes close to fractures and coarse ones far from them; the method uses iterative octree refinement of a structured hexahedral mesh. Once the mesh is generated, the UDFM formulates permeability tensors of meshes that intersect fractures. The permeability of each intersected mesh is calculated using the fracture apertures and orientation. The fracture network generation and upscaling by the UDFM algorithm is implemented in the DFN modeling suite dfnWorks (Hyman et al., 2015). Lastly, the created upscaled permeability distribution in the tetrahedral meshes was converted into cubic meshes such that it has a consistent mesh structure with the previously generated porous media zone. The generated continuum scale permeability distribution representing FR is then coupled with porous media (US and WR), finalizing the 3D HSC model as shown in Fig. 3c. The detailed illustration of the completed model is provided in Fig. S8.

4. Numerical simulation and analyses for 3D DNAPLs transport

4.1. Model setup

The spatiotemporal behaviors of DNAPLs penetrating through US, WR, and FR were evaluated in the 3D HSC model. Assuming a hypothetical situation where the DNAPLs were spilled from a point source

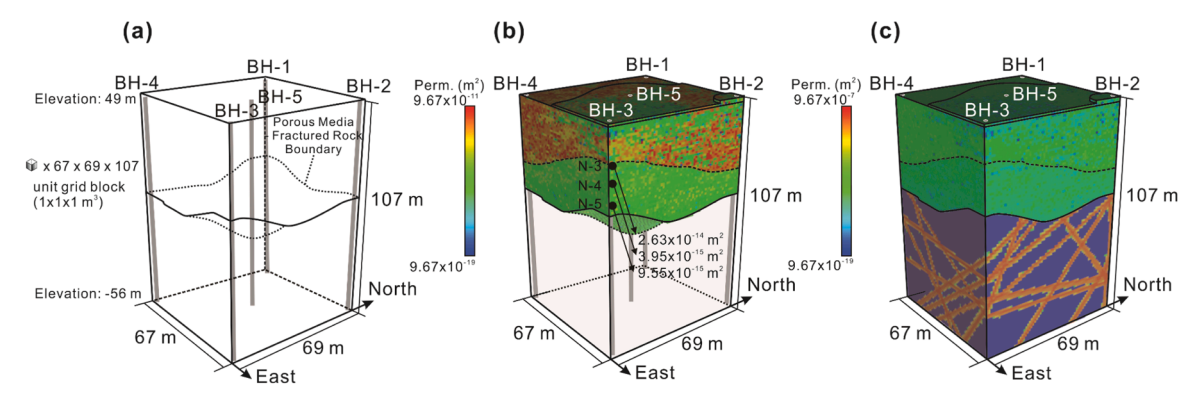


Fig. 3. (a) 3D model domain and Heterogeneous permeability distribution for (b) porous media (US + WR) and (c) both porous media and fractured rock (US + WR + FR).

located in US, downward migrations of the DNAPLs through both porous media (US and WR) and fractured rock (FR) were investigated. The top boundary of the 3D HSC model was assigned to the atmospheric condition (101.3 kPa) and the bottom boundary was assigned to the no-flow boundary (903.5 kPa), representing intact and impermeable rock (Table 1). Accordingly, the vertical pressure hydrostatically increased from the atmospheric pressure to 903.5 kPa at the bottom. The lateral boundaries were assigned a hydrostatically increasing pressure, which was invariant with the time. The groundwater depth was assigned at 22 m without a hydraulic gradient, referring to the relatively insignificant effect of the horizontal groundwater flow observed at the Deokso test-bed.

The DNAPLs, where the source was located at 24 m east, $50 \sim 54$ m north, and 34 m elevation, were spilled at a constant rate of 0.04 m³/ day during 35 years (Fig. 4a). After the spilling ceased, natural DNAPLs migration through US, WR, and FR was observed during the next 65 years. The density and viscosity of the DNAPLs were 1130 kg/m³ and 0.013 Pa·s under atmospheric pressure, respectively [34]; here, the values resemble the properties of the polychlorinated biphenyl (PCB) class of DNAPLs, manifesting intermediate values in density and viscosity among the values of various types of DNAPLs (e.g. creosote, coal tar, and chlorinated solvent). The DNAPLs migration through the US zone creates a 3-phase fluid system in the subsurface where air-DNAPLs-water phases coexist in porous media. For the relative permeability of the air-DNAPLs-water phases, an empirical 3-phase relative permeability function known as the modified Stone I model was adopted [6]. For capillary pressure, DNAPLs-water was the greatest at matrix in FR (ranging from 1 kPa to 10 kPa), intermediate at porous media (ranging from 0.5 kPa to 5 kPa), and the smallest at fractures (ranging from 0.1 kPa to 1 kPa) [59]. Hysteresis effects on both relative permeability and capillary pressure and phase transition/chemical reaction between water-air-DNAPLs phase (i.e. dissolution, vaporization, and condensation) were not considered in this study. Finally, the DNAPLs migration through US, WR, and FR was simulated with CMG IMEX multiphase simulator [12].

4.2. Case scenarios for sensitivity study

A series of scenarios were designed to assess uncertainties of the field-data-integrated 3D HSC model and to identify influencing factors on DNAPLs distribution. Among numerous factors, hydrogeological and geostructural properties of WR and FR were focused on (Table 2). In WR, the DNAPLs migration is affected by a composition of irregular geological substrates (generally classified in regolithic soil, saprolite, and saprock), which result from a complex interplay of geological and

Table 1Model parameters and assigned values for the 3-D HSC model.

| Model parameter | Assigned value | | | | |
|--|--|------------------------------------|--------------|--|--|
| Number of elements | x-direction: 67, y-direction: 69, z-direction: 107 | | | | |
| Size of each element (m) | $\Delta x, \Delta y, \Delta z = 1$ | $\Delta x, \Delta y, \Delta z = 1$ | | | |
| Temperature (°C) | 20 (constant) | | | | |
| Pressure (kPa) | Top | Top Bottom | | | |
| | 101.3 | 903.5 | | | |
| Groundwater depth (m) | 22 | | | | |
| DNAPLs density (kg/m ³) | 1130 | | | | |
| DNAPLs spilling rate (m ³ /day) | 0.04 | | | | |
| DNAPLs source location | (x, y, z): (24, 50, 34), (24, 51, 34), (24, 52, 34), | | | | |
| | (24, 53, 34), (24, 54, 34) | | | | |
| | where the origin (0,0,0) located on the BH-4 side corner | | | | |
| | | | | | |
| Simulation period (years) | DNAPL spilling ceased | Simulation end | | | |
| | 35 | 100 | | | |
| Relative permeability curve | Modified Stone I function ([6]) | | | | |
| Capillary pressure curve (kPa) | Porous media | Fractured | Fractures | | |
| sapinary pressure curve (kr tr) | 1 010 do media | rock matrix | 114004105 | | |
| | $0.5 \sim 5$ | $1\sim 10$ | $0.1 \sim 1$ | | |

weathering processes [39,42]. To describe the variability in WR, the effect of permeability anisotropy (k_z/k_x) and intra-structure of WR were investigated. Accounting for isotropic permeability $(k_z/k_x = 1)$ in WR as base-case, the k_x/k_x varied to 0.25 (Scenario 1) and 4 (Scenario 2), covering from horizontally to vertically developed weathering environments [37,46,52,61]. In addition, different from the mono structure of WR in the base-case 3D HSC model, a dual structure assuming a sharp permeability transition in WR was designed at Scenario 3 (Fig. S9b). Here, WR was bisected to upper and lower parts where the mean permeability of the upper WR ($k_{\rm u} = 1.82\,k_{\rm WR}$) was 10 times greater than lower WR ($k_l = 0.182 k_{WR}$) while maintaining the mean permeability of WR equal to the base-case k_{WR} (=3.4 ×10⁻¹⁴ m²). In Scenario 4, to account for a smoother transition of geological substrates, WR was divided into four parts, upper ($k_u = 1.82 k_{WR}$), middle-upper ($k_{mu} = 1.27 k_{WR}$), middle-lower ($k_{\rm ml}=0.73~k_{\rm WR}$), and lower ($k_{\rm l}=0.182~k_{\rm WR}$) WR while maintaining the entire mean permeability as k_{WR} (Fig. S9c). In Scenario 5 and Scenarios 6, the effect of an impermeable clay-layer was investigated, reflecting the genesis of the clay-layer during weathering process [57]; a single clay-layer with 1 m thickness ($k_{clay}=1.0 \times 10^{-16} \text{ m}^2$) was located at the bottom of and in the middle of the WR, respectively (Fig. S9d, S9e).

For FR, matrix permeability (k), fracture aperture size (λ), and fracture + matrix mean porosity (ϕ) were varied. In FR, the preferential migration of DNAPLs through fractures is influenced by a degree of transmissibility into the surrounding matrix [48]. To assess the effect of the transmissibility, the scenarios varying matrix *k* from $1.0 \times 10^{-18} \, \mathrm{m}^2$ (base-case), 1.0×10^{-16} m² (Scenario 7) to 1.0×10^{-20} m² (Scenario 8) were designed (Table 2). Subsequently, the fracture aperture size (λ), a well-known prominent factor for the DNAPLs migration in FR [44], was varied. The λ in the base-case was 8.0 mm, larger than an ordinary single fracture because fractures at the test-bed were mainly detected as a bundle, forming wide fractures. To assess the impact of λ reducing from a size of bundled fracture to a single fracture, scenarios reducing λ to 4 mm (Scenario 9) and 1 mm (Scenario 10) were designed. Finally, the uncertainty by employing ϕ from the neutron-porosity data was assessed by varying mean ϕ in FR. The mean ϕ in the base-case was 7.5%, while the experimental porosities measured from the cores at the depth of FR (N-6: 5.3%; N-7: 0.22%) were smaller than the mean ϕ . Therefore, smaller mean ϕ cases were considered in Scenario 11 (ϕ : 4.0%) and Scenario 12 (ϕ : 1.0%), respectively.

4.3. Spatial moment analysis

For all scenarios, the spatiotemporal distribution of DNAPLs in each of US, WR, and FR was quantitatively analyzed by spatial moment analysis [8,11,21,24,38]. For a 3D space composed of x, y, and z axes orthogonal to each other, the 3D spatial moment of DNAPLs within each media D (D = [US, WR, FR, Total]) can be calculated as the following equations:

$$\mathbf{M}_{ijk} = \iiint_{D} \phi(x, y, z) \, \rho(x, y, z) \, S(x, y, z) x^{i} y^{j} z^{k} dx dy dz$$
 [2]

$$M_x = \frac{M_{100}}{M_{000}}, \ M_y = \frac{M_{010}}{M_{000}}, \ \text{and} \ M_z = \frac{M_{001}}{M_{000}},$$
 [3]

$$\begin{split} M_{xx} &= \frac{M_{200}}{M_{000}} - \left(\frac{M_{100}}{M_{000}}\right)^2, \ M_{yy} = \frac{M_{020}}{M_{000}} - \left(\frac{M_{010}}{M_{000}}\right)^2, \ \text{and} \ M_{zz} \\ &= \frac{M_{002}}{M_{000}} - \left(\frac{M_{001}}{M_{000}}\right)^2 \end{split} \tag{4}$$

where the ϕ , ρ , and S are the porosity, density, and saturation of each grid-block, respectively. The i,j, and k no less than 0 indicate the degree of x, y, and z values, respectively where i+j+k determines the degree of the spatial moment. The 0th spatial moment (i.e. i+j+k=0) in zone D directly indicates the amount of DNAPLs mass in zone D (M_{000}^{P}).

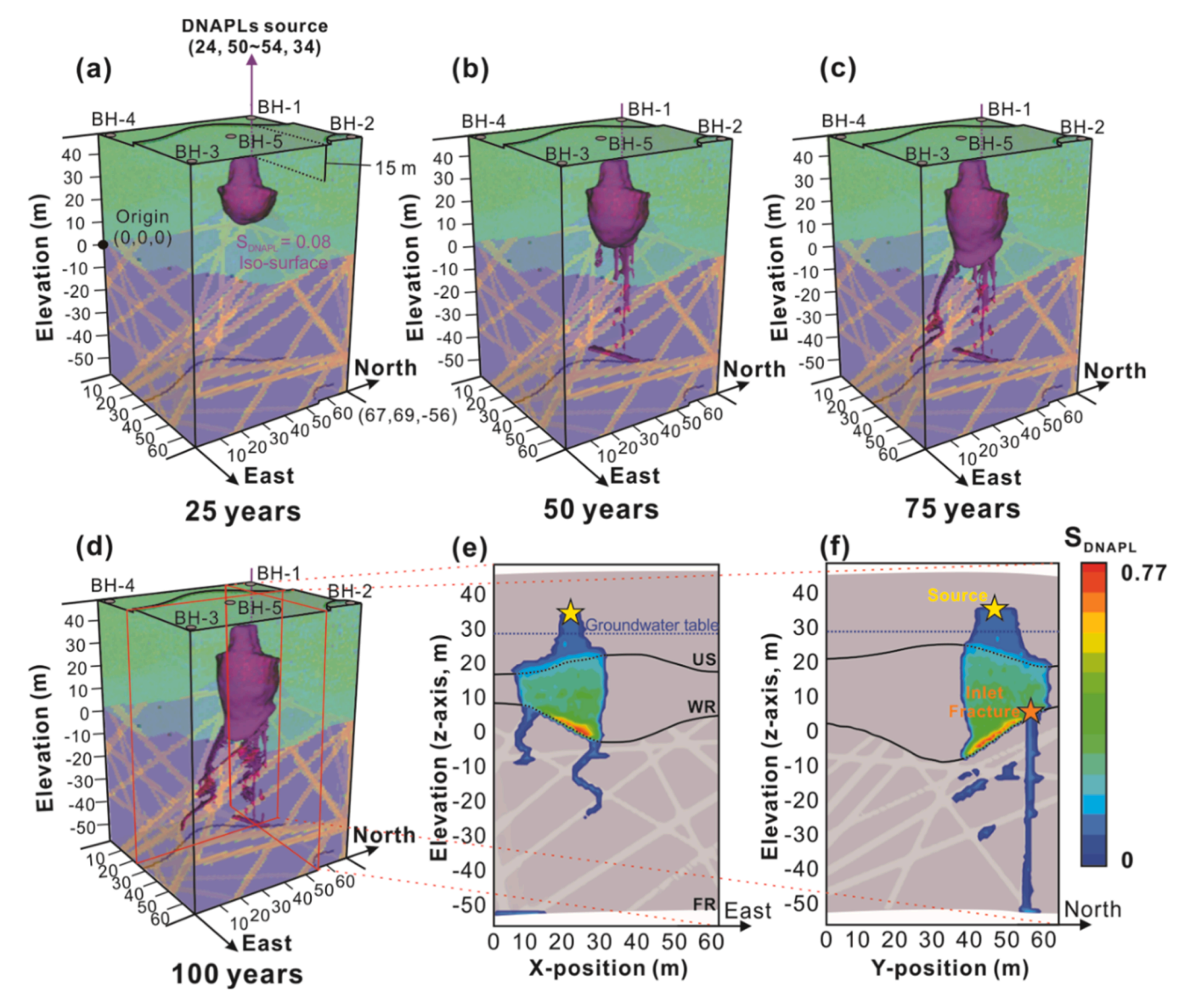


Fig. 4. 3D DNAPLs migration for (a) 25 years, (b) 50 years, (c) 75 years, and (d) 100 years in simulation time, and 2D cross-sectional DNAPLs distribution derived from 100 years for (e) W-E (x-axis) and (f) S-N (x-axis) planes. Yellow stars denote the DNAPLs source location and an orange star denotes the location of the inlet fracture that DNAPLs initially enter.

Likewise, the 1st $(M_x^D, M_y^D, \text{ and } M_z^D)$ and the 2nd spatial moment $(M_{xx}^D, M_{yy}^D, \text{ and } M_{zz}^D)$ indicate the center of DNAPLs mass and the variance of DNAPLs distribution, respectively.

5. Base case

5.1. Spatiotemporal behavior of DNAPLs in US, WR, and FR

The 3D spatiotemporal distributions of DNAPLs with an iso-surface of 0.08 saturation were visualized in 25-year intervals (Fig. 4a–d). At 25 years, DNAPLs mostly resided in US and above WR (Fig. 4a). The DNAPLs plume migrated downward due to gravitational force, while simultaneously spreading toward the northwest on the sloped US-WR boundary; the thickness of WR was thin approaching the northwest. At 50 years, a portion of the DNAPLs reaching the WR-FR boundary invaded FR deeply (Fig. 4b). The invasion occurred rapidly when the DNAPLs entered the nearly vertical fractures. Once arriving at the base of FR, the DNAPLs accumulated and laterally spread toward both east and west. In contrast to the DNAPLs migration in FR which is highly

dependent on the fracture geometry, the DNAPLs plume in WR was almost uniformly distributed by forming a convex DNAPLs pool. At 75 years, the pooled DNAPLs above the WR-FR boundary slid down toward the center and entered other fractures dipping toward the southwest (Fig. 4c). The DNAPLs continuously spread on the WR-FR boundary until 100 years (Fig. 4d).

To investigate the migration patterns of DNAPLs influenced by geologic discontinuities, 2D cross-sections intersecting the DNAPLs source to W-E and S-N directions were delineated at 100 years (Figs. 4e and 4f); for the sake of simplicity, distance along W-E and S-N directions are labeled as X- and Y-positions, respectively. The simulation results highlighted that most DNAPLs in US migrated to WR while the DNAPLs whose saturation was under 0.1 were residually trapped in US. The geologic discontinuity of the US-WR boundary more significantly impacted downgoing DNAPLs than the groundwater table. The DNAPLs were stagnant and spread laterally above the US-WR boundary due to the difference in permeability. The spread led to a broader area of contamination by the DNAPLs in WR. The DNAPLs plumes then accumulated on the WR-FR boundary, developing the DNAPLs pool where its saturation reached approximately 0.77. A portion of the pooled DNAPLs,

Table 2Sensitivity scenarios for weathered rock and fractured rock properties.

| Scenarios | permeability anisotropy of WR | Structure of WR | FR matrix permeability | Fracture aperture | FR mean porosity | |
|--------------|-------------------------------------|---|------------------------|-------------------|------------------|--|
| | (k_z/k_x) | (mean $k_{\rm WR} = 3.4 \times 10^{-14} \rm m^2$) | (m^2) | (mm) | (%) | |
| WR | | | | | | |
| | or WR permeability anisotropy | | | | | |
| Base-case | 1 | Mono structure (k_{WR}) | 1.0×10^{-18} | 8.0 | 7.5 | |
| 1 | 0.25 | Mono structure (k_{WR}) | 1.0×10^{-18} | 8.0 | 7.5 | |
| 2 | 4 | Mono structure (k_{WR}) | 1.0×10^{-18} | 8.0 | 7.5 | |
| Scenarios fe | or WR structure | | | | | |
| Base-case | 1 | Mono structure (k_{WR}) | 1.0×10^{-18} | 8.0 | 7.5 | |
| 3 1 | 1 | Dual structure | 1.0×10^{-18} | 8.0 | 7.5 | |
| | | $(k_{\rm u} = 1.82 \ k_{\rm WR},$ | | | | |
| | $k_{\rm l} = 0.18 \ k_{\rm WR}$) | | | | | |
| 4 | 1 | Quadruple structure | 1.0×10^{-18} | 8.0 | 7.5 | |
| | | $(k_{\rm u}=1.82~k_{ m WR},k_{ m mu}=1.37~k_{ m WR},k_{ m ml}=0.75~k_{ m WR},k_{ m l}=$ | | | | |
| | | $0.18 k_{WR}$) | | | | |
| 5 | 1 | Basal Clay layer | 1.0×10^{-18} | 8.0 | 7.5 | |
| | | $(k_{\rm clay} = 1.0 \times 10^{-16} \mathrm{m}^2)$ | | | | |
| 6 | 1 | Middle Clay layer | $1.0 	imes 10^{-18}$ | 8.0 | 7.5 | |
| | | $(k_{\rm clay} = 1.0 \times 10^{-16} \mathrm{m}^2)$ | | | | |
| FR | | • | | | | |
| Scenarios f | or matrix permeability | | | | | |
| Base-case | 1 | Mono structure (k_{WR}) | 1.0×10^{-18} | 8.0 | 7.5 | |
| 7 | 1 | Mono structure (k_{WR}) | $1.0 	imes 10^{-16}$ | 8.0 | 7.5 | |
| 8 | 1 | Mono structure (k_{WR}) | $1.0 	imes 10^{-20}$ | 8.0 | 7.5 | |
| Scenarios fe | or fracture aperture size | | | | | |
| Base-case | 1 | Mono structure (k_{WR}) | $1.0 	imes 10^{-18}$ | 8.0 | 7.5 | |
| 9 | 1 | Mono structure (k_{WR}) | 1.0×10^{-18} | 4.0 | 7.5 | |
| 10 | 1 | Mono structure (k_{WR}) | $1.0 	imes 10^{-18}$ | 1.0 | 7.5 | |
| Scenarios fe | or mean porosity (fracture and matr | <u>'ix)</u> | | | | |
| Base-case | 1 | Mono structure (k_{WR}) | 1.0×10^{-18} | 8.0 | 7.5 | |
| 11 | 1 | Mono structure (k_{WR}) | 1.0×10^{-18} | 8.0 | 4.0 | |
| 12 | 1 | Mono structure (k_{WR}) | $1.0 	imes 10^{-18}$ | 8.0 | 1.0 | |

enveloping a part of the WR-FR boundary, invaded FR through an inlet fracture (orange star in Fig. 4f). Once entering the nearly vertical inlet fracture, the DNAPLs directly reached the base of FR. In summary, the influence of the geologic discontinuity and slope of media boundaries, location of inlet fractures, and fracture orientation controlling DNAPLs migration were investigated on the 3D HSC model.

5.2. Quantification of DNAPLs mass distribution

The DNAPLs mass that existed in each media D (M_{000}^D , D=[US, WR, FR, Total]) within the 3D HSC model was evaluated over time (Fig. 5a). The M_{000}^{Total} (red solid-line) was increased to 561.8 tons until the DNAPLs spill ceased at 35 years, and decreased to 508.3 tons at 100 years

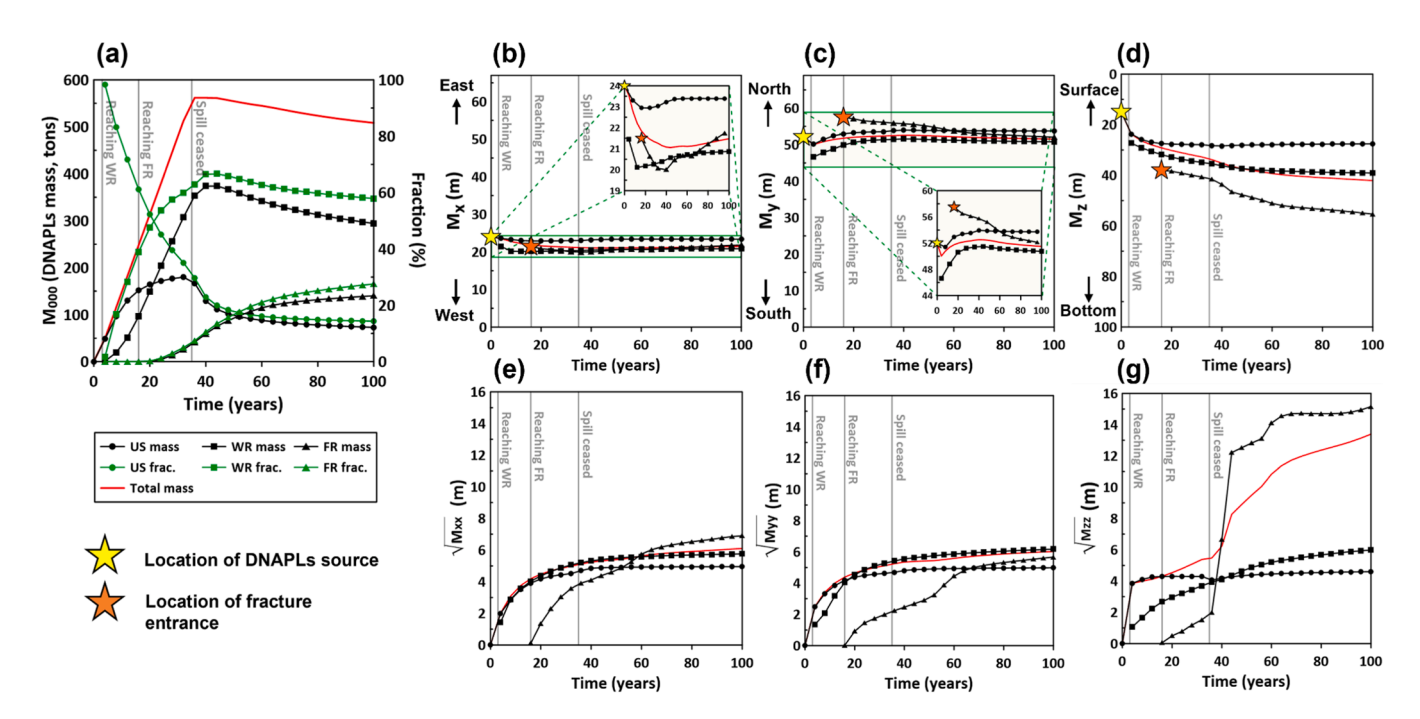


Fig. 5. Temporal changes in the (a) zeroth (M_{000}^D) , (b-d) first $(M_x^D, M_y^D, \text{ and } M_z^D)$, and (e-g) second $(M_{xx}^D, M_{yy}^D, \text{ and } M_{zz}^D)$ spatial moments during 100-year DNAPLs migration. Entirely, black lines with circular, rectangular, and triangular symbols denote US, WR, and FR spatial moments, respectively. Red solid lines denote spatial moments for the entire media. Green symbolic lines in a are fractions of DNAPL mass.

primarily due to lateral migration of DNAPLs out of the modeling domain through high permeable fractures. The M_{000}^{US} (--) increased to 179.9 tons until 35 years, and decreased asymptotically to 73.0 tons at 100 years. The final DNAPLs mass that remained in US as residually trapped ganglia accounted for 13% of the total DNAPLs mass. On the other hand, moveable DNAPLs in US migrated to WR. The M_{000}^{WR} (---) increased by 373.7 tons at 40 years ($M_{000}^{US} < M_{000}^{WR}$ after 21 years), dominantly accounting for 68% of the total mass. Dominance in WR was prolonged to 100 years, although the mass fraction decreased to 59% due to the continued migration of DNAPLs to FR. The DNAPLs arrived FR at 16 years for the first time, and then, M_{000}^{FR} (---) gradually increased to 130.0 tons until 100 years, accounting for 28% of the total mass.

Next, temporal changes in the center of mass $(M_x^D, M_y^D, \text{ and } M_z^D)$ in Fig. 5b-d) and the variance $(M_{xx}^D, M_{yy}^D, \text{ and } M_{zz}^D \text{ in Fig. 5e-g)}$ for DNAPLs distribution were tracked in each x- (W-E), y- (S-N), and z- (vertical) direction, respectively. Note that the M_x^{Total} , M_y^{Total} , and M_z^{Total} at the time (t) = 0 represent the location of DNAPLs source (see yellow stars in Fig. 5b-d). Additionally, the M_{xx}^D , M_{yy}^D , and M_{zz}^D were expressed in a reduced dimension with a distance unit (m) by taking a square root, for a more intuitive comparison (i.e. $\sqrt{M_{xx}^D},\,\sqrt{M_{yy}^D},$ and $\sqrt{M_{zz}^D}$). Temporally, the M_x^{Total} showed a larger variability than both M_x^{Total} and M_y^{Total} , highlighting a vertically dominant DNAPLs migration (red solid-line in Fig. 5b-d). While both M_x^{Total} (24.0-21.3 m, Fig. 5b) and M_v^{Total} (50.0–51.8 m, Fig. 5c) varied within a relatively small range, M_z^{Total} varied from 15.0 to 40.1 m (Fig. 5d). Similarly, both $\sqrt{M_{xx}^{Total}}$ and $\sqrt{M_{yy}^{Total}}$ varied within less than 4.2 m (Figs. 5e and 5f), but the $\sqrt{M_{zz}^{Total}}$ increased from 0 to 13.7 m (Fig. 5g). As well, the variability of DNAPLs distribution depended on geologic media. In US, the M_x^{US} and M_y^{US} only varied within ranges of approximately 0.7 m and 3.9 m, respectively (- in Figs. 5b and 5c). The M_z^{US} that started from the DNAPLs source (depth of 15.0 m), deepened until reaching the US-WR boundary (27.6 m). In WR ($-\blacksquare$), the variability of M_x^{WR} and M_y^{WR} became greater than those in US. The M_x^{WR} and M_y^{WR} varied approximately 1.3 m and 4.9 m. The M_z^{WR} deepened from the vicinity of the US-WR boundary (27. 6 m) to the WR-FR boundary (39.1 m) (Fig. 5d). In FR (), the center of mass (M_x^{FR}, M_y^{FR}, and M_z^{FR}) and variances ($\sqrt{M_{xx}^{FR}}$, $\sqrt{M_{yy}^{FR}}$, and $\sqrt{M_{zz}^{FR}}$) varied differently, due to the distinct behavior of DNAPLs migrating through fractures. After DNAPLs reached FR (see orange stars in Fig. 5b-d), the M_z^{FR} deepened from a depth of 39.7-53.8 m. Concurrently, the $\sqrt{M_{77}^{FR}}$ dramatically increased from 2.0 m (36 years) to

12.2 m (44 years), implicating that DNAPLs penetrated through the nearly vertical fracture (Fig. 5g). In short, the quantification results presented dominant DNAPLs mass in WR, and irregular spatiotemporal distribution of DNAPLs by each geological medium.

5.3. Effects of geologic discontinuity and preferential fractures on DNAPLs migration

The centers of mass to the x- and y-direction $(M_{x-y}^D, D=[US, WR, FR])$ were plotted on the elevation contour of US-WR and WR-FR boundaries (Fig. 6); here, the arrow-head line trails movement of M_{x-y}^D dependent on the discontinuity in geological media. Additionally, the horizontal spreadings of DNAPLs were plotted as sky-blue circles at time t=4 (16 for FR), 20, 40, 60, 80, and 100 years. The radius of the circle is represented by the larger values between $\sqrt{M_{xx}^D}$ and $\sqrt{M_{yy}^D}$.

The variation of $M_{x\text{-}y}^{US}$, $M_{x\text{-}y}^{W\ R}$, and $M_{x\text{-}y}^{FR}$ was influenced by the boundaries of contacting geologic media. The $M_{x\text{-}y}^{US}$ initially located at the DNAPLs source (yellow star) moved toward the north following the down-slope of the US-WR boundary and approached the coordinate (x = 23.4, y = 53.7) at 100 years (Fig. 6a). Concurrently, the radii of the circles were increased up to 4.98 m. In WR, the $M_{x,y}^{W\,R}$ originated at $(x=21.4,\,y=46.6)$. At early time, the $M_{x,y}^{W\,R}$ moved toward the northwest under the influence of the US-WR boundary but slightly turned back to the south when the DNAPLs reached the WR-FR boundary sloping toward the southeast (Fig. 6b). While the DNAPLs progressed toward the north, the DNAPLs plume accumulated the wide area above the WR-FR boundary similar to the observation in Figs. 4e and 4 f. Eventually, the DNAPLs reached the inlet fracture (orange star) at the WR-FR boundary. Once the DNAPLs entered FR, the MFR moved toward the south, reflecting the primary dip direction of fractures (Fig. 6c). Here, due to rapid migration of DNAPLs through highly permeable fractures, the maximum variance at 100 years was the largest in FR (6.9 m) among US, WR, and FR. In summary, DNAPLs exhibited distinct migration characteristics across the geologic media. Again, a critical role of both geologic discontinuity and preferential fracture network governing the DNAPLs migration and distribution in the 3D HSC model was found. In the following section, accordingly, the influence of the characteristics of weathered rock and fractured rock, on subsurface DNAPLs behavior was investigated.

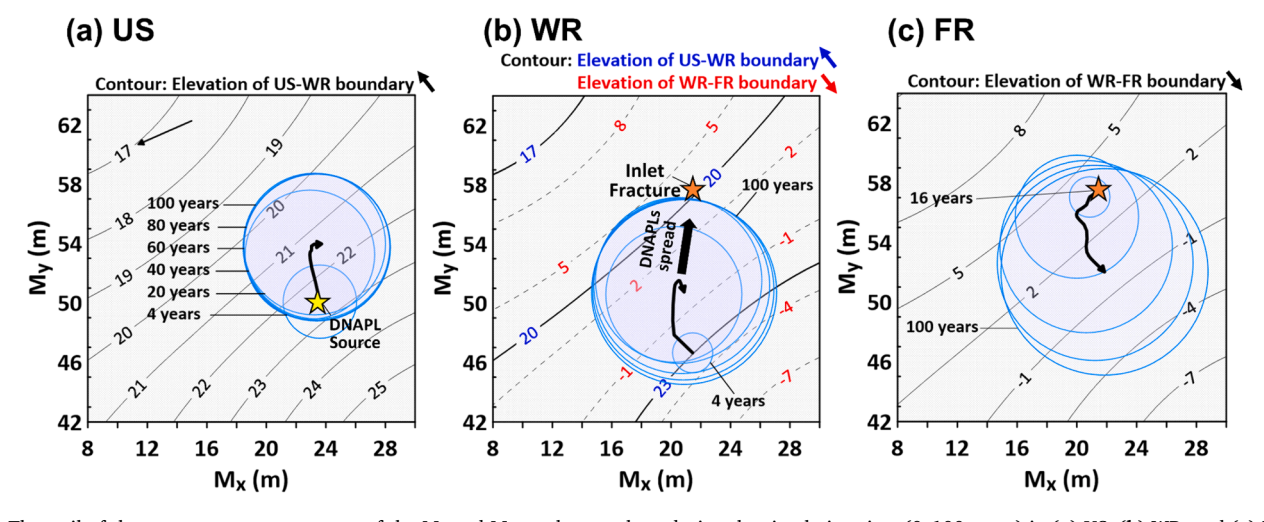


Fig. 6. The trail of the contemporary movement of the M_x and M_y on the x-y plane during the simulation time (0–100 years) in (a) US, (b) WR, and (c) FR. The contours in each figure represent the elevations of US-WR and WR-FR boundaries.

6. Effects of weathered rock and fractured rock characteristics

6.1. DNAPLs mass distribution by weathered rock characteristics: permeability anisotropy and structural discontinuity

For different weathered rock (WR) properties (Scenario (S) 1–6 in Table 2), the temporal variation in DNAPLs mass (Fig. 7a) and the mass distribution in each of US, WR, and FR (Fig. 7b–d) were evaluated. At t=100 years, the visualizations of DNAPLs distribution in S1, S2, S3, and S6 were depicted (Fig. 7e–h).

The S1 and S2, which assigned the anisotropy $k (k_z/k_x)$ of WR by 0.25 and 4.0 respectively, revealed the greatest impact on both M_{000}^{FR} and M_{000}^{Total} (Fig. 7a). In S1 ($k_z/k_x = 0.25$), M_{000}^{FR} was relatively insignificant having values less than 42.2 tons, due to weak migration of DNAPLs from WR to FR (Fig. 7e). Whereas, in S2 ($k_z/k_x = 4.0$) characterizing strong vertical migration of DNAPLs through WR, M₀₀₀ rapidly increased from 0 to 182.8 tons until 44 years (Fig. 7a). As seen, more DNAPLs vertically dispersed in WR with less horizontal spread, and thus, the amount of DNAPLs arrived in FR increased (Fig. 7f). Eventually, M_{000}^{FR} decreased to 130.6 tons in 100 years. The decrease of M_{000}^{FR} in the late time was due to the DNAPLs escaping out of the domain of interest through fractures. The S3 and S4 showed the equal mean permeability (k) but different structural discontinuities in WR. The M_{000}^{FR} in S3 (dual k structure illustrated in Fig. S9b) was smaller than in S4 (quadruple k structure illustrated in Fig. S9c), indicating the DNAPLs migration was impeded more in WR with less complexity and a sharp discontinuity in k structure. The S5 and S6, where the clay-layer is located at the bottom (Fig. S9d) and in the middle of WR (Fig. S9e), highlighting noticeable difference in M_{000}^{FR} . While M_{000}^{FR} in S5 (the basal clay-layer) increased from 0 to 126.1 tons at t = 100 years, that in S6 (the middle clay-layer) minimally increased to 5.7 tons. This suggested that the intercepting clay-layer further away from FR could be more effective at preventing the DNAPLs entry into FR (Fig. 7h).

The temporal mass fraction of DNAPLs distributed in US, WR, and FR for each scenario was depicted on a ternary diagram (S1 and S2 in Fig. 7b; S3 and S4 in Fig. 7c; S5 and S6 in Fig. 7d), compared with BC. The trail of mass fraction in S1 positioned slightly above that of BC (US: 0.22, WR: 0.68, and FR: 0.10 in 100 years), reflecting the DNAPLs mass mostly resided in both US and WR due to the low k_z/k_x (Fig. 7e). Whereas, the mass fraction in S2 with high k_z/k_x approached the lower right-side of BC (US: 0.14, WR: 0.43, and FR: 0.43 in 100 years), reflecting the greater entry of DNAPLs to FR (Fig. 7f). Both the trails of mass fraction in S3 (dual k structure) and S4 (quadruple k structure) were shifted upward compared to BC, indicating more DNAPLs mass in WR (Fig. 7c); the mass fraction of S3 and S4 ended up at US: 0.1, WR: 0.69, FR: 0.21, and US: 0.11, WR: 0.62, FR: 0.27, respectively. The mass fraction in WR was larger at S3 (0.69) than S4 (0.62), because the sharper k discontinuity lead to more horizontal spread of DNAPLs, and thus, impeded the vertical migration of DNAPLs more effectively. Finally, when a clay-layer was positioned at the bottom of WR (S5), the mass fraction of DNAPLs in WR was slightly increased (US: 0.13, WR: 0.64, FR: 0.23) compared to BC (Fig. 7d). However, when the clay-layer was placed in the middle of WR (S6), most of DNAPLs resided in WR with minimal entry to FR (US: 0.14, WR: 0.85, FR: 0.01). In summary, throughout the WR characteristics, the permeability anisotropy (k_x/k_y) was most influential on DNAPLs fate. Notably, when the k_z/k_x was high, more DNAPLs entered high permeable fractures, presenting the most challenging condition for DNAPLs remediation. Both discontinuous kstructures and clay-layers in WR served as an obstacle impeding the vertical migration of DNAPLs. Particularly, a clay-layer placed in the middle of WR prevented nearly 100% of the DNAPLs entry to FR.

6.2. Horizontal DNAPLs migration and spread by weathered rock characteristics

The change of WR characteristics through S1–S6 affected the entire $M_{x,y}^{WR}$, $M_{x,y}^{WR}$, and $M_{x,y}^{FR}$, leading to large uncertainty in predicting DNAPLs

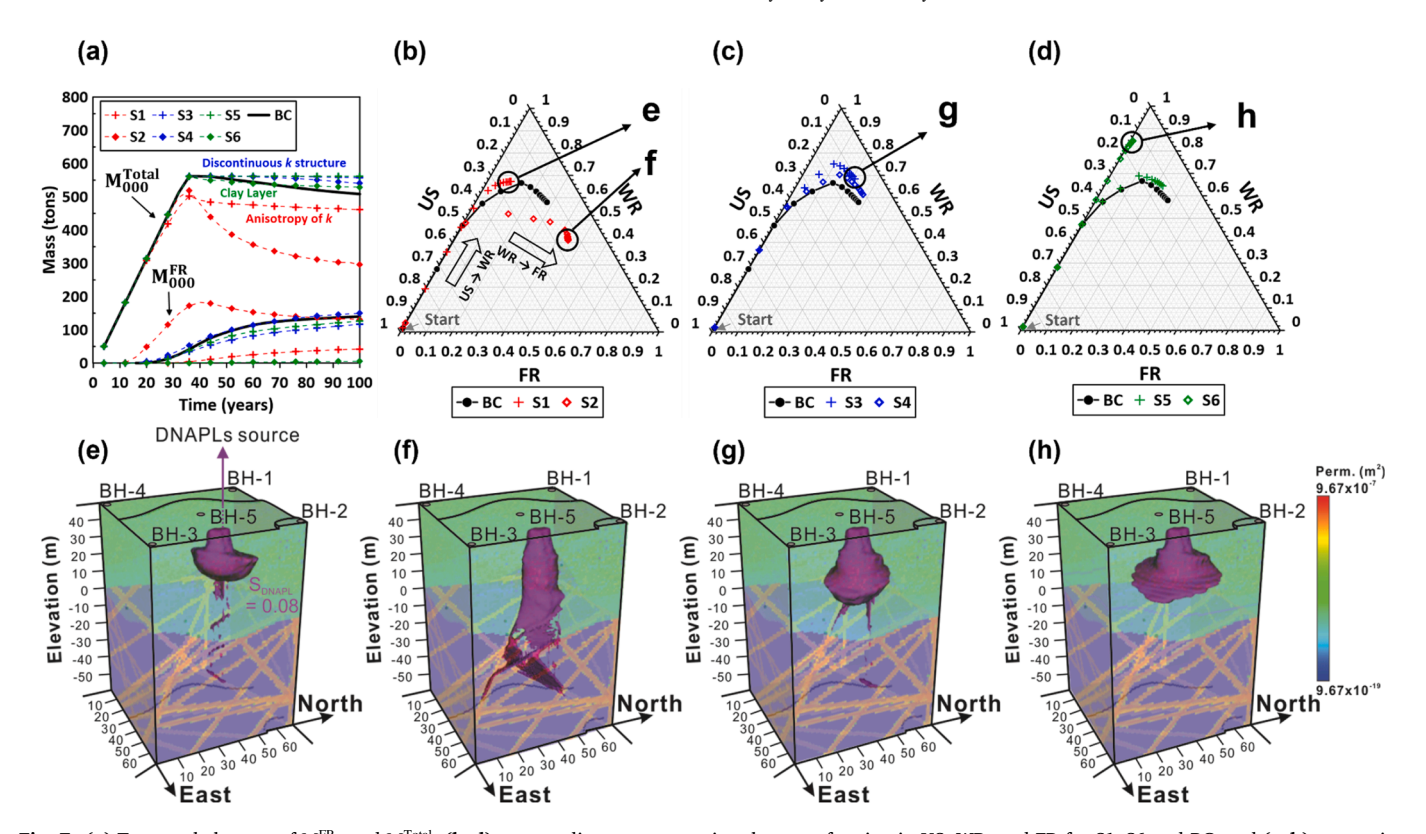


Fig. 7. (a) Temporal changes of M_{000}^{FR} and M_{000}^{Total} , (b–d) ternary diagrams presenting the mass fraction in US, WR, and FR for S1–S6 and BC, and (e–h) supporting visualizations of S1, S2, S3, and S6 at t = 100 years.

migration (Fig. 8a-c). In US, M_{x-v} from all WR scenarios moved toward the north above the US-WR boundary, equally influenced by the slope of the boundary (Fig. 8a). The displacement of $M_{x,y}^{US}$ was the maximum in S1 (4.68 m) and the minimum in S2 (1.58 m), reflected by the effect of reduced and enhanced k_z/k_x in WR, respectively. The M_{x-y}^{US} for S3, S4, S5, and S6 (scenarios of WR k structure and a clay-layer) showed intermediate displacement. Similar to US, in WR, $M_{x,y}^{W\,R}$ in S1–S6 equally moved northward, although the starting points of $M_{x,y}^{W\,R}$ differed depending on the horizontal spread of DNAPLs due to anisotropic k and structural discontinuity (Fig. 8b). For instance, S1 with low k_z/k_x showed a large horizontal spread of DNAPLs above the US-WR boundary, and thus, the starting point of $M_{x-y}^{W\ R}$ was distanced from the DNAPLs source (yellow star in Fig. 8a). Whereas, the starting point in S2 with high k_z/k_x was close to the DNAPLs source. The displacement of MWR increased proportionally to the distance to the starting point; the displacement of M_xwR was greatest (4.75 m) in S1 and smallest in S2 (0.67 m). In addition, the M_{X-V} for S3, S4, S5, and S6 showed intermediate displacement. The starting points and horizontal variations of $M_{x-y}^{W\ R}$ lead to critical differences in DNAPLs migration in FR. For example, the DNAPLs that spread wider in S1 encountered the new fracture inlet at (x = 8.5, y = 62.7)(brown star, Figs. 8b and 8c). However, in S2-S6, the DNAPLs entered FR through the inlet fracture close to the DNAPLs source (orange star). Finally, after DNAPLs entered inlet fractures, M_{x-v} for all scenarios moved windingly to the south or southeast (opposite from M_{x-y}^{US} and M_{x-y} yWR) following to major dip direction of fractures (Fig. 8c).

The degree and asymmetry of the spreading DNAPLs in both x- and y-directions were assessed by the comparisons of $\sqrt{M^D_{xx}}$ and $\sqrt{M^D_{yy}}$ at every 4-year intervals (Fig. 8d–f). Both $\sqrt{M^D_{xx}}$ and $\sqrt{M^D_{yy}}$ increased over time

while leaning to either x- or y-axes, indicating that DNAPLs spread continuously and asymmetrically. In US, the degree and asymmetry were relatively insignificant for all scenarios; the maximum variance (at t = 100 years) was approximately 3.68 m in S2 to 6.16 m in S1 (Fig. 8d). In WR, most DNAPLs spread symmetrically except for S1 with low $k_{\rm Z}/k_{\rm x}$ (Fig. 8e). Nevertheless, the maximum spreading differed in large variations among the scenarios compared to US; S2 (from 1.30 m to 4.46 m by time) and S6 (from 1.34 m to 8.99 m by time) was smallest and largest, respectively. Such large variations in WR influenced both spreading patterns and the amount of DNAPLs in FR (Fig. 8f). The asymmetry of DNAPLs in FR was greatest in S1, where the DNAPLs entered the distinct inlet fractures as shown in Fig. 8c. Nevertheless, the asymmetries in FR were entirely developed toward the x-direction, indicating the significant effect of the fracture network distribution.

6.3. DNAPLs mass distribution, migration, and spread by fractured rock characteristics: permeability, aperture size, and porosity

The mass distribution, migration, and spread of DNAPLs with varying FR characteristics (S7–S12 in Table 2) were quantified (Fig. 9a–c), along with the visualization of DNAPLs distribution at t=100 years for S8 (Fig. 9d), S10 (Fig. 9e), and S12 (Fig. 9f), respectively. Since the FR conditions influenced the DNAPLs behavior in both upper US and WR insignificantly, only the results in FR were focused.

The mean matrix k of FR in S7 and S8 was two orders of magnitude higher $(1.0 \times 10^{-16} \,\mathrm{m}^2)$ and lower $(1.0 \times 10^{-20} \,\mathrm{m}^2)$ than one in BC. Even though matrix k was changed, the temporal variation of $\mathrm{M}_{000}^{\mathrm{FR}}$ and $\mathrm{M}_{000}^{\mathrm{Total}}$ in S7 and S8 showed not much difference from ones in BC (Fig. 9a). In FR, the transmissibility due to changes in matrix k exert no significant

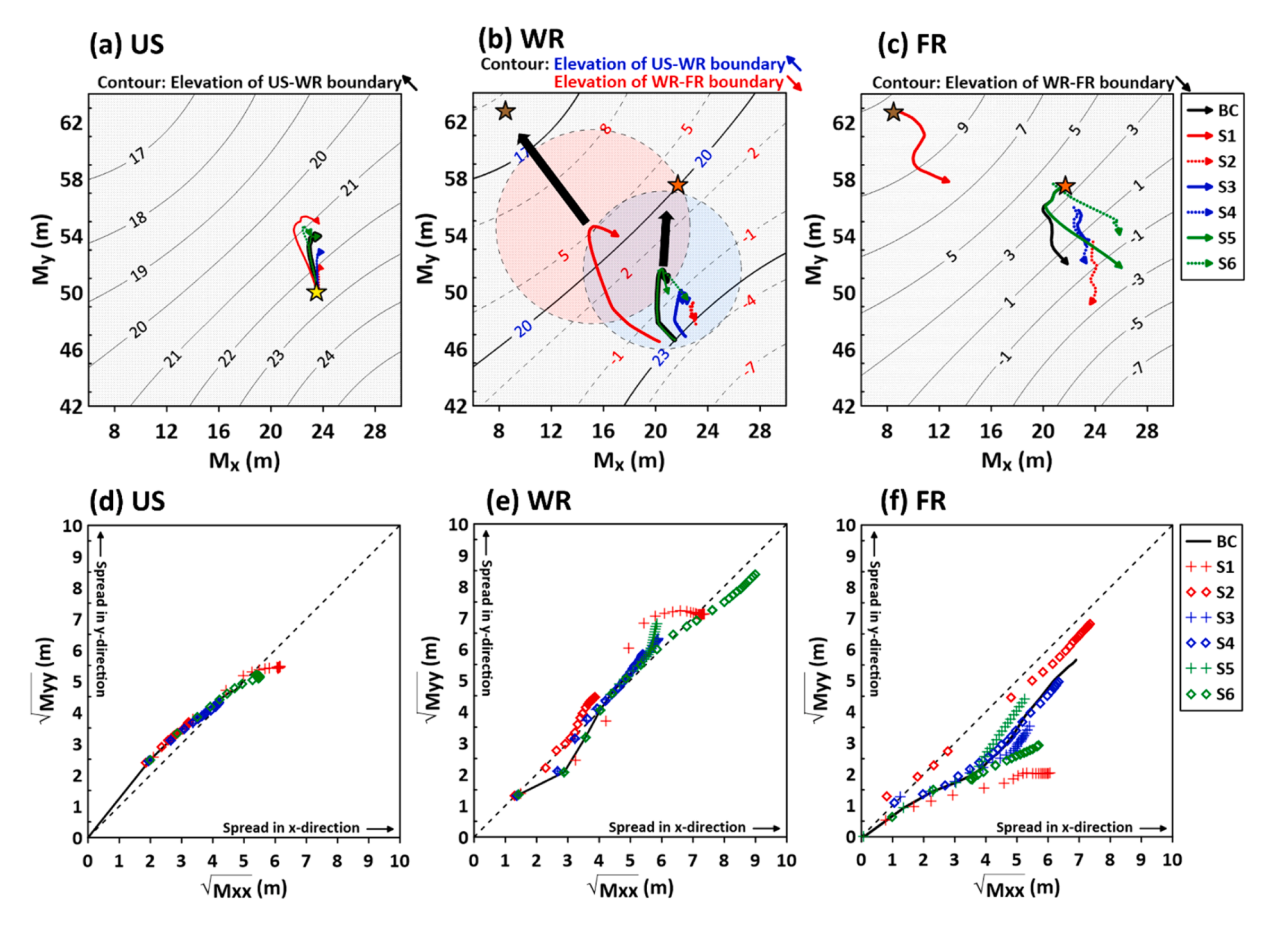


Fig. 8. Temporal changes of the horizontal (both x- and y-direction) center of mass (a-c) and variances of DNAPLs (d-f) for S1–S6 in each geologic media. The contours in a-c represent the elevation of contacting media boundaries. Yellow stars denote the location of DNAPLs source. Red and blue translucent circles in b indicate the DNAPLs spread of which radii are $\sqrt{M_{xx}^{WR}}$ of S2 and BC at t = 100 years.

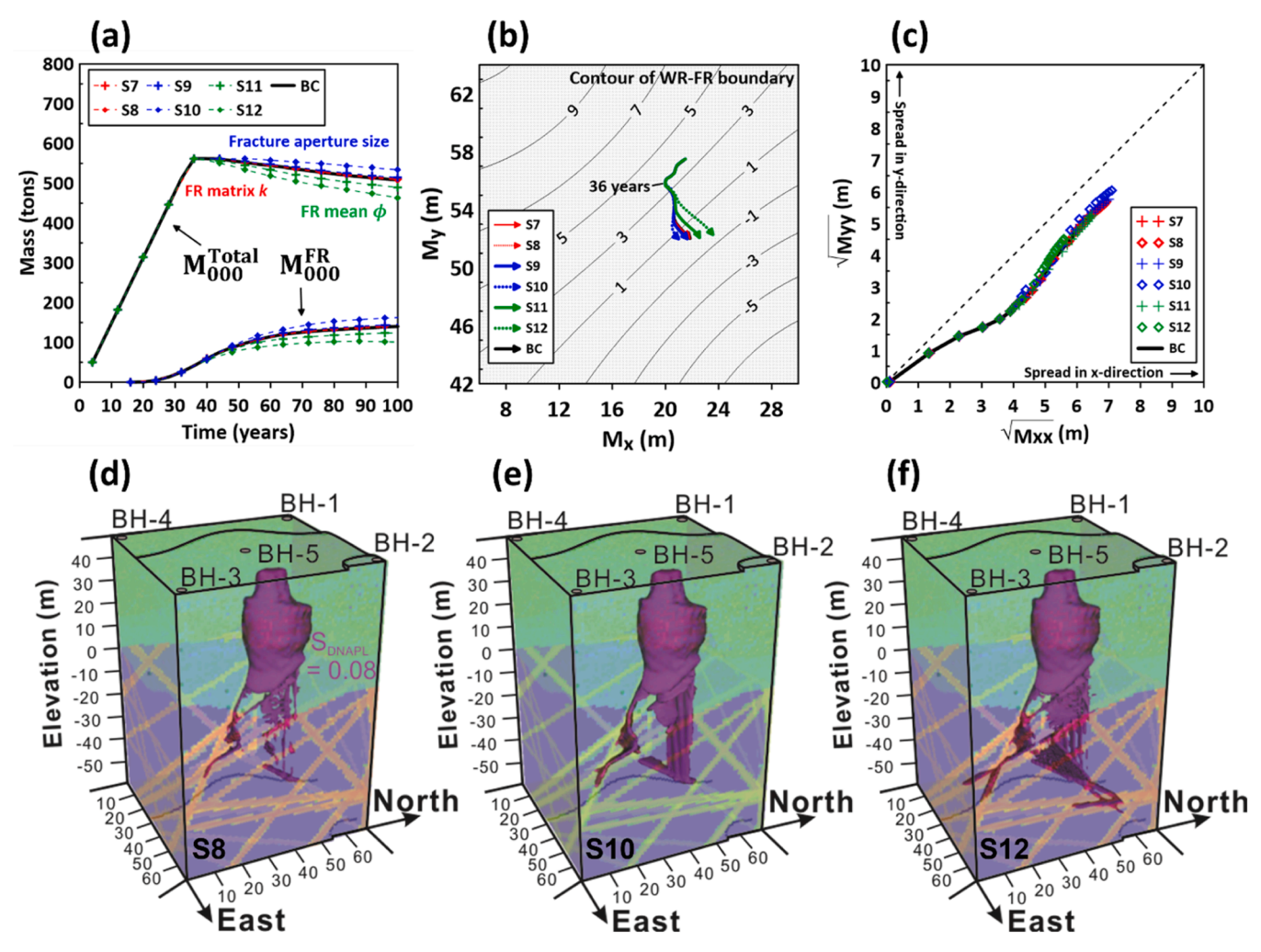


Fig. 9. (a) DNAPLs mass in FR and total model domain, and (b and c) the horizontal migration and spread in FR in base-case and S7–12. Red, blue, and green symbolic lines represent the results of scenarios varying matrix permeability (S7 and S8), fracture aperture size (S9 and S10), and mean ϕ (S11 and S12), respectively. (d-f) supporting visualizations of S8, S10, and S12 at t = 100 years.

changes of DNAPLs distribution and migration through fracture pathways; permeability of fracture is still large enough to serve as preferential pathways for DNAPLs (Fig. 9d). However, fracture aperture (λ) size and mean porosity (ϕ) affected both M_{000}^{FR} and M_{000}^{Total} . When λ decreased from 8 mm (the size of a bundle of fractures) in BC, to 4 mm and 1 mm (the size of a single fracture) in S9 and S10 respectively, both the M_{000}^{FR} and M_{000}^{Total} increased (Fig. 9a). As the λ decreased, the M_{000}^{FR} increased because more DNAPLs were impeded and stored within the fractures as shown in Fig. 9e. As a result, the final M_{000}^{Total} was increased by a maximum of 4.8% compared to that in BC. In contrast to the λ size, both M_{000}^{Total} and M_{000}^{FR} decreased proportionally to decrease in ϕ (Fig. 9a). Compared to BC (ϕ = 7.5%), the M_{000}^{Total} and M_{000}^{FR} in S11 (ϕ = 4.0%) and S12 (ϕ = 1.0%) became smaller at late time; the final M_{000}^{Total} decreased by a maximum of 8.8%. In small ϕ , the flow velocity in fracture increases, accelerating DNAPLs transport outside the model domain; DNAPLs distribute in complicated fracture networks and reach the fracture outlet in the eastern boundary (Fig. 9f). As a result, DNAPLs mass in the 3D HSC model was decreased (Fig. 9a).

The horizontal migration and spread patterns of DNAPLs while changing the FR conditions were evaluated (Fig. 9b–c). The $M_{x-y}^{\rm FR}$ in S7–S12 moved along the identical path until 36 years and then diverged (Fig. 9b). Nevertheless, their y-positions at 100 years were almost the same because the DNAPLs penetrated through the same major fracture elongated across the x-direction (y = 52.0). For the same reason, the

DNAPLs spread asymmetrically leaning toward the x-direction in all S7–12, showing slight deviations from BC (Fig. 9c).

In summary, uncertainties that arise from the characteristics of FR were increased in the order of matrix k, λ , and mean ϕ in the 3D HSC model. The change of matrix k did not affect the prediction of overall DNAPLs behavior. The changes of λ and ϕ resulted in maximum differences of 4.8% and 8.8% in the final $M_{000}^{\rm Total}$, respectively, compared to that in BC. However, the results of horizontal migration and spread of DNAPLs exhibited almost identical characteristics throughout S7–S12 because of their similar migration pathways, indicating the dominant effect of fracture orientation and distribution on DNAPLs migration. Finally, the overall results from the hydrogeological properties in FR showed less impact than the geostructural properties in WR, on the DNAPLs migration.

7. Implications and limitations

Previously, many studies focused on understanding DNAPLs flow and transport mechanisms within either a single porous or fractured rock medium, in part, due to the lack of a method capable of effectively integrating the distinctive hydraulic characteristics of both geological media. Recent advancements in computational-mesh upscaling methodologies, such as UDFM adopted in this study, enabled the integration of these properties and a unified analysis of DNAPLs behavior across both media. Additionally, the previous studies often relied on pore-,

laboratory-, and pilot-scale experiments and numerical simulations with simplified and controlled setups. Although the approaches could provide detailed descriptions through available data, the small-scale observation was often insufficient to reflect the practical and natural behavior of DNAPLs at the field-scale including heterogeneity, anisotropy, and irregularity in hydrogeological and geostructural conditions. In this study, the development of the 3D HSC numerical model based on systematic field investigations allowed for more complex and realistic geological settings, including irregular stratifications and heterogeneity resulting from weathering and geological evolution processes; these often play a critical role but are typically overlooked at small-scales.

The 3D numerical simulations and analyses using the HSC model enabled quantitative evaluation for field-scale spatiotemporal distribution and migration of DNAPLs. The results of base-case and sensitivity scenarios successfully captured the characteristic behavior of DNAPLs in US, WR, and FR as well as the effect of transition between these media. Stagnance and spreading of DNAPLs above the boundaries, the limited entrance of DNAPLs into FR through sparse inlet fractures, and the preferential transport in networks of the major fractures were highlighted. The sensitivity scenario results also underscored the considerable influence of WR. For example, the anisotropy and discontinuity of kin WR on the DNAPLs fate and transport exceeded the effects of FR properties, determining the location of fracture inlets that DNAPLs migrated into. In addition, a single clay-rich layer interlayered in WR effectively prevented the DNAPLs entry into FR. To date, the significance of WR in DNAPLs contamination has been underexplored in previous research due to the challenges associated with preserving the in situ condition of WR during drilled core sampling and logging, as well as the loss of information during experimental or model simplification [42]. The findings in this study regarding WR effects suggest the necessity for a detailed evaluation of WR with pedologic and geologic evolutionary perspectives, in line with recent observations at the practical DNAPLs contaminated site [28,32].

This study successfully integrated multiple geological media based on high-resolution field data, while exploring media transition and WR effects on the field-scale DNAPLs contamination. Nevertheless, the study requires further investigation and refinement. The feasibility and accuracy of the DNAPLs migration should be validated through subsequent demonstration and experiment at the real contaminated site. Additionally, the current model simplified DNAPLs contaminant to a single chemical component to focus on evaluating the WR and FR properties. However, DNAPLs in practice often consist of complex mixtures, introducing uncertainties in density, viscosity, and other chemo-physical properties. Future research should address multi-component DNAPLs behavior and the complex interaction of the components. Furthermore, the biochemical parameters including redox conditions and microbial activities, which play a crucial role in DNAPLs attenuation and remediation, should be considered to enhance the model performance and predictability.

8. Conclusion

The field-scale distribution and migration of subsurface DNAPLs were predicted and interpreted through the 3D HSC numerical model, for the first time, integrating both porous (US and WR) and fractured rock media (FR). For realistic realization, diverse field observation data (lithologic, hydrogeologic, petrophysical, and fracture data) from both in situ and laboratory experiments were integrated. In the 3D HSC model, the spatiotemporal distribution during hypothetic DNAPLs contamination of 100 years was quantitatively evaluated by numerical simulations and rigorous momentum analyses. As a result, the influence of the characteristics of each medium and the non-linear transition between geologic media were delineated. In addition, the significance of WR characteristics (e.g. permeability anisotropy, clay-rich layer, or discontinuous strata) on DNAPLs contamination was explored through sensitivity studies, aligning with recent observations at the actual

contaminated site [28,32]. The findings suggest the need for a more detailed evaluation of WR with pedologic and geologic evolutionary perspectives during DNAPL site evaluation, which have been often overlooked.

Further research and refinement are required to validate the accuracy of DNAPLs migration, especially considering the complex mixtures of DNAPLs in practical scenarios. Future investigations should also consider biochemical parameters related to redox conditions and microbial activities to enhance the model predictability and performance. With these future improvements, it is expected that one can readily incorporate the new data into the proposed 3D HSC model to advance interpretation of field-scale subsurface DNAPLs contamination processes and expand the parametric sensitivity analyses. While the study primarily focused on the effect of six geostructural and hydrogeologic parameters within WR and FR, the scope of the investigation can be extended to other subjects, such as effects of soil particle size, organic matters, microbes, capillarity, and fluctuations in groundwater table, as well as optimal installation of remediation facilities, and the characteristics of fracture morphology [3,30,49,62,65].

Environmental implication

Dense non-aqueous phase liquids (DNAPLs) contamination has become a global, unresolved conundrum due to its widespread industrial application and complex dynamics in the subsurface. DNAPLs are poorly soluble in water and have a higher density than water. Therefore, they infiltrate deeply under groundwater table, contaminating multiple aquifers and geological media at various depths. At the actual DNAPLs contaminated site, their fate and transport can be disturbed by irregular geostructures and hydrologic properties arising from weathering process. This study highlighted less explored aspects of field-scale DNAPLs behavior in weathered rock, by developing a 3D high-resolution subsurface characteristic numerical model.

CRediT authorship contribution statement

Taehoon Kim Conceptualization, Data Curation, Resources, Software, Formal Analysis, Validation, Visualization, Methodology, Writing – original draft. **Weon Shik Han** Conceptualization, Supervision, Resources, Writing – review & editing, Funding acquisition. **Seonkyoo Yoon** Methodology, Data curation, Writing – review & editing. **Peter K. Kang** Supervision, Writing- review & editing. **Jehyun Shin** Resources, Investigation. **Myung Jin Nam** Resources, Investigation.

Declaration of Competing Interest

The authors declare that they have no known competing financial interests or personal relationships that could have appeared to influence the work reported in this paper.

Data availability

Data will be made available on request.

Acknowledgment

This research was supported by the Subsurface Environmental Management (SEM) project through the Korea Environmental Industry and Technology Institute (KEITI) funded by the Ministry of Environment [No. RS-2023-00230833), by the National Research Foundation of Korea (NRF) funded through Ministry of Science and ICT [No. 2023R1A2C1003168), and by Korea Institute of Energy Technology Evaluation and Planning (KETEP) through the Korea government MOTIE [No. 2021040101003B]. PKK and SY acknowledge the support by the National Science Foundation under Grant No. EAR-2046015.

Appendix A. Supporting information

Supplementary data associated with this article can be found in the online version at doi:10.1016/j.jhazmat.2023.132711.

References

- Adamson, D.T., McDade, J.M., Hughes, J.B., 2003. Inoculation of a DNAPL source zone to initiate reductive dechlorination of PCE. Environ Sci Technol 37 (11), 2525–2533. https://doi.org/10.1021/es020236y.
- [2] Aken, B.V., Doty, S.L., 2009. Transgenic plants and associated bacteria for phytoremediation of chlorinated compounds. Biotechnol Genet Eng Rev 26 (1), 43-64. https://doi.org/10.5661/bger-26-43.
- [3] An, S., Kim, K., Woo, H., Yun, S.-T., Chung, J., Lee, S., 2022. Coupled effect of porous network and water content on the natural attenuation of diesel in unsaturated soils. Chemosphere 302, 134804. https://doi.org/10.1016/j. chemosphere.2022.134804.
- [4] An, S., Woo, H., Kim, S.H., Yun, S.-T., Chung, J., Lee, S., 2023. Complex behavior of petroleum hydrocarbons in vadose zone: A holistic analysis using unsaturated soil columns. Chemosphere 326, 138417. https://doi.org/10.1016/j. chemosphere 2023 138417.
- [5] Aydin-Sarikurt, D., Dokou, Z., Copty, N.K., Karatzas, G.P., 2016. Experimental investigation and numerical modeling of enhanced DNAPL solubilization in saturated porous media. Water Air Soil Pollut 227, 1–16. https://doi.org/10.1007/ s11270-016-3136-0.
- [6] Aziz, K., Settari, A., 1979. Petroleum reservoir simulation. 1979. Applied Science Publ. Ltd., London, UK.
- [7] Barbee, G.C., 1994. Fate of chlorinated aliphatic hydrocarbons in the vadose zone and ground water. Groundw Monit Remediat 14 (1), 129–140. https://doi.org/ 10.1111/j.1745-6592.1994.tb00098.x.
- [8] Basu, N.B., Rao, P., Falta, R.W., Annable, M.D., Jawitz, J.W., Hatfield, K., 2008. Temporal evolution of DNAPL source and contaminant flux distribution: Impacts of source mass depletion. J Contam Hydrol 95 (3–4), 93–109. https://doi.org/ 10.1016/j.jconhyd.2007.08.001.
- [9] Berkowitz, B., 2002. Characterizing flow and transport in fractured geological media: A review. Adv Water Resour 25 (8–12), 861–884.
- [10] Chapman, S.W., Parker, B.L., Cherry, J.A., Aravena, R., Hunkeler, D., 2007. Groundwater-surface water interaction and its role on TCE groundwater plume attenuation. J Contam Hydrol 91 (3–4), 203–232. https://doi.org/10.1016/j. iconhvd.2006.10.006.
- [11] Christ, J.A., Lemke, L.D., Abriola, L.M., 2005. Comparison of two-dimensional and three-dimensional simulations of dense nonaqueous phase liquids (DNAPLs): Migration and entrapment in a nonuniform permeability field. Water Resour Res 41 (1). https://doi.org/10.1029/2004WR003239.
- [12] CMG, 2020. IMEX user guide, black oil & unconventional simulator. Computer Modeling Group Calgary, Alberta, Canada.
- [13] Cochennec, M., Davarzani, H., Davit, Y., Colombano, S., Ignatiadis, I., Masselot, G., et al., 2022. Impact of gravity and inertia on stable displacements of DNAPL in highly permeable porous media. Adv Water Resour 162, 104139. https://doi.org/10.1016/j.advwatres.2022.104139.
- [14] Cohen, R.M., & Mercer, J.W., 1993, DNAPL site evaluation: SK Smoley.
- [15] Colombano, S., Davarzani, H., Van Hullebusch, E., Huguenot, D., Guyonnet, D., Deparis, J., et al., 2021. Comparison of thermal and chemical enhanced recovery of DNAPL in saturated porous media: 2D tank pumping experiments and two-phase flow modelling. Sci Total Environ 760, 143958. https://doi.org/10.1016/j. scitotenv.2020.143958.
- [16] Costa, A., 2006. Permeability-porosity relationship: A reexamination of the Kozeny-Carman equation based on a fractal pore-space geometry assumption. Geophys Res Lett 33 (2).
- [17] Dennis, I., Pretorius, J., Steyl, G., 2010. Effect of fracture zone on DNAPL transport and dispersion: a numerical approach. Environ Earth Sci 61, 1531–1540. https:// doi.org/10.1007/s12665-010-0468-8.
- [18] Du Plessis, J.P., Masliyah, J.H., 1991. Flow through isotropic granular porous media. Transp Porous Media 6 (3), 207–221. https://doi.org/10.1007/
- [19] Engelmann, C., Lari, K.S., Schmidt, L., Werth, C.J., Walther, M., 2021. Towards predicting DNAPL source zone formation to improve plume assessment: Using robust laboratory and numerical experiments to evaluate the relevance of retention curve characteristics. J Hazard Mater 407, 124741. https://doi.org/10.1016/j.jhazmat.2020.124741.
- [20] Ersahin, S., Gunal, H., Kutlu, T., Yetgin, B., Coban, S., 2006. Estimating specific surface area and cation exchange capacity in soils using fractal dimension of particle-size distribution. Geoderma 136 (3–4), 588–597. https://doi.org/ 10.1016/j.geoderma.2006.04.014.
- [21] Freyberg, D.L., 1986. A natural gradient experiment on solute transport in a sand aquifer: 2. Spatial moments and the advection and dispersion of nonreactive tracers. Water Resour Res 22 (13), 2031–2046. https://doi.org/10.1029/ WR022i013p02031.
- [22] Gandhi, R.K., Hopkins, G.D., Goltz, M.N., Gorelick, S.M., McCarty, P.L., 2002. Full-scale demonstration of in situ cometabolic biodegradation of trichloroethylene in groundwater 2. Comprehensive analysis of field data using reactive transport modeling. Water Resour Res 38 (4), 11–11-11-18. https://doi.org/10.1029/2001WR000380.

- [23] Giraud, Q., Gonçalvès, J., Paris, B., Joubert, A., Colombano, S., Cazaux, D., 2018. 3D numerical modelling of a pulsed pumping process of a large DNAPL pool: In situ pilot-scale case study of hexachlorobutadiene in a keyed enclosure. J Contam Hydrol 214, 24–38.
- [24] Han, W.S., Lee, S.Y., Lu, C., McPherson, B.J., 2010. Effects of permeability on CO₂ trapping mechanisms and buoyancy-driven CO₂ migration in saline formations. Water Resour Res 46 (7). https://doi.org/10.1029/2009WR007850.
- [25] Hao, Z., Xu, H., Feng, Z., Zhang, C., Zhou, X., Wang, Z., et al., 2021. Spatial distribution, deposition flux, and environmental impact of typical persistent organic pollutants in surficial sediments in the Eastern China Marginal Seas (ECMSs). J Hazard Mater 407, 124343. https://doi.org/10.1016/j.ihazmat.2020.124343.
- [26] Huling, S.G., Weaver, J.W., 1991. Ground water issue: dense nonaqueous phase liquids. US Environmental Protection Agency, https://doi.org/10.1016/j. iconbvd 2018 05 005
- [27] Imhoff, P.T., Mann, A.S., Mercer, M., Fitzpatrick, M., 2003. Scaling DNAPL migration from the laboratory to the field. J Contam Hydrol 64 (1–2), 73–92. https://doi.org/10.1016/S0169-7722(02)00106-7.
- [28] ITRC, 2015. Integrated DNAPL Site Characterization and Tools Selection (ISC-1)). Interstate Technology & Regulatory Council, DNAPL Site Characterization Team, Washington, D.C. Retrieved from.
- [29] Kavanaugh, M.C., Rao, P., Abriola, L., Cherry, J., Destouni, G., Falta, R., et al., 2003. The DNAPL remediation challenge: Is there a case for source depletion? US Environmental Protection Agency, National Risk Management Research Laboratory..
- [30] Kim, T., Han, W.S., Piao, J., Kang, P.K., Shin, J., 2022. Predicting remediation efficiency of LNAPLs using surrogate polynomial chaos expansion model and global sensitivity analysis. Adv Water Resour 163, 104179. https://doi.org/ 10.1016/j.advwatres.2022.104179.
- [31] Kueper, B.H., Frind, E.O., 1991. Two-phase flow in heterogeneous porous media: 1. Model development. Water Resour Res 27 (6), 1049–1057. https://doi.org/ 10.1029/91WR00266.
- [32] Leahy, K., Baldock, J., Johnson, K., 2017. The role of geological structure and weathering in contaminant fate and transport in fractured bedrock at two sites in the UK. Q J Eng Geol Hydrogeol 50 (3), 287–300. https://doi.org/10.1144/ qjegh2016-126.
- [33] Lebedeva, M.I., Brantley, S.L., 2017. Weathering and erosion of fractured bedrock systems. Earth Surf Process Landf 42 (13), 2090–2108. https://doi.org/10.1002/ esp.4177.
- [34] Lerner, D., Kueper, B., Wealthall, G., Smith, J., & Leharne, S., 2003, An illustrated handbook of DNAPL transport and fate in the subsurface.
- [35] Lorz, C., Heller, K., Kleber, A., 2011. Stratification of the regolith continuum-a key property for processes and functions of landscapes. Z Geomorphol 55 (3), 277–292. https://doi.org/10.1127/0372-8854/2011/0055S3-0062.
- [36] Lowe, D.F., Oubre, C.L., Ward, C.H., 1999. Surfactants and cosolvents for NAPL remediation a technology practices manual. Crc Press., Boca Raton, Fla.
- [37] Lu, N., Godt, J.W., 2013. Hillslope hydrology and stability. Cambridge University Press., Cambridge, U.K.
- [38] Natarajan, N., Kumar, G.S., 2018. Spatial moment analysis of multispecies contaminant transport in porous media. Environ Eng Res 23 (1), 76–83. https://doi.org/10.4491/eer.2016.147.
- [39] National Academies of Sciences Engineering and Medicine, 2020. Characterization, modeling, monitoring, and remediation of fractured rock. National Academies Press
- [40] Pankow, J.F., Cherry, J.A., 1996. Dense chlorinated solvents and other DNAPLs in groundwater: History, behavior, and remediation. Waterloo Press,, Portland, Or.
- [41] Philippe, N., Davarzani, H., Colombano, S., Dierick, M., Klein, P.-Y., Marcoux, M., 2020. Experimental study of the temperature effect on two-phase flow properties in highly permeable porous media: Application to the remediation of dense non-aqueous phase liquids (DNAPLs) in polluted soil. Adv Water Resour 146, 103783. https://doi.org/10.1016/j.advwatres.2020.103783.
- [42] Phillips, J.D., Pawlik, Ł., Šamonil, P., 2019. Weathering fronts. Earth Sci Rev 198, 102925. https://doi.org/10.1016/j.earscirev.2019.102925.
- [43] Remy, N., Boucher, A., Wu, J., 2009. Applied geostatistics with SGeMS: A user's guide. Cambridge University Press,.
- [44] Reynolds, D., Kueper, B., 2002. Numerical examination of the factors controlling DNAPL migration through a single fracture. Groundwater 40 (4), 368–377. https://doi.org/10.1111/j.1745-6584.2002.tb02515.x.
- [45] Reynolds, D.A., Kueper, B.H., 2004. Multiphase flow and transport through fractured heterogeneous porous media. J Contam Hydrol 71 (1–4), 89–110. https://doi.org/10.1016/j.jconhyd.2003.09.008.
- [46] Riebe, C.S., Hahm, W.J., Brantley, S.L., 2017. Controls on deep critical zone architecture: A historical review and four testable hypotheses. Earth Surf Process Landf 42 (1), 128–156. https://doi.org/10.1002/esp.4052.
- [47] Sahimi, M., 2011. Flow and transport in porous media and fractured rock: from classical methods to modern approaches. John Wiley & Sons,. https://doi.org/ 10.1002/9783527636693.
- [48] Sandve, T.H., Berre, I., Nordbotten, J.M., 2012. An efficient multi-point flux approximation method for discrete fracture–matrix simulations. J Comput Phys 231 (9), 3784–3800. https://doi.org/10.1016/j.jcp.2012.01.023.
- [49] Shi, J., Yang, Y., Lu, H., Xi, B., Li, J., Xiao, C., et al., 2021. Effect of water-level fluctuation on the removal of benzene from soil by SVE. Chemosphere 274, 129796. https://doi.org/10.1016/j.chemosphere.2021.129796.
- [50] Shin, J., Hwang, S., Jung, S.H., Han, W.S., Son, J.-S., Nam, M.J., et al., 2022. Development of site-scale conceptual model using integrated borehole methods:

- systematic approach for hydraulic and geometric evaluation. Water 14 (9), 1336. https://doi.org/10.3390/w14091336.
- [51] Slough, K., Sudicky, E., Forsyth, P., 1999. Importance of rock matrix entry pressure on DNAPL migration in fractured geologic materials. Groundwater 37 (2), 237–244. https://doi.org/10.1111/j.1745-6584.1999.tb00979.x.
- [52] Sommer, M., Halm, D., Weller, U., Zarei, M., Stahr, K., 2000. Lateral podzolization in a granite landscape. Soil Sci Soc Am J 64 (4), 1434–1442. https://doi.org/ 10.2136/sssaj2000.6441434x.
- [53] Sweeney, M.R., Gable, C.W., Karra, S., Stauffer, P.H., Pawar, R.J., Hyman, J.D., 2020. Upscaled discrete fracture matrix model (UDFM): an octree-refined continuum representation of fractured porous media. Comput Geosci 24, 293–310.
- [54] Taylor, G., Eggleton, R.A., 2001. Regolith geology and geomorphology. John Wiley & Sons., Chichester, U.K.
- [55] Van der Meij, W., Temme, A.J., Lin, H., Gerke, H.H., Sommer, M., 2018. On the role of hydrologic processes in soil and landscape evolution modeling: concepts, complications and partial solutions. Earth Sci Rev 185, 1088–1106. https://doi. org/10.1016/j.earscirev.2018.09.001.
- [56] VanderKwaak, J., Sudicky, E., 1996. Dissolution of non-aqueous-phase liquids and aqueous-phase contaminant transport in discretely-fractured porous media. J Contam Hydrol 23 (1–2), 45–68. https://doi.org/10.1016/0169-7722(95)00087-
- [57] Velde, B.B., Meunier, A., 2008. The origin of clay minerals in soils and weathered rocks. Springer Science & Business Media,. https://doi.org/10.1007/978-3-540-75634-7.
- [58] Walsh, J.B., Brace, W., 1984. The effect of pressure on porosity and the transport properties of rock. J Geophys Res Solid Earth 89 (B11), 9425–9431. https://doi. org/10.1029/JB089iB11p09425.

- [59] Wang, X.-H., Li, L., Wang, M., Liu, Z.-F., Shi, A.-F., 2020. A discrete fracture model for two-phase flow involving the capillary pressure discontinuities in fractured porous media. Adv Water Resour 142, 103607. https://doi.org/10.1016/j. adwatres.2020.103607.
- [60] Wilson, J.L., 1990, Laboratory Investigation of Residual Liquid Organics from Spills, leaks and the Disposal of Hazardous Wastes in Groundwater, EPA/600/ S6–90/004.
- [61] Yokota, S., Iwamatsu, A., 2000. Weathering distribution in a steep slope of soft pyroclastic rocks as an indicator of slope instability. Developments in Geotechnical Engineering. Elsevier,, pp. 187–198. https://doi.org/10.1016/S0165-1250(00) 80016-4.
- [62] Yoon, S., Hyman, J.D., Han, W.S., Kang, P.K., 2023. Effects of dead-end fractures on non-Fickian transport in three-dimensional discrete fracture networks. e2023JB026648 J Geophys Res: Solid Earth 128 (7). https://doi.org/10.1029/ 2023JB026648
- [63] Yu, H., Shin, J., Kim, B., Cho, A., Lee, G.H., Pyun, S., et al., 2022. Geophysical exploration and well logging for the delineation of geological structures in a Testbed. J Soil Groundwater Environ 27 (S1), 19–33. https://doi.org/10.7857/ JSGE.2022.27.5.019.
- [64] Zheng, F., Gao, Y., Sun, Y., Shi, X., Xu, H., Wu, J., 2015. Influence of flow velocity and spatial heterogeneity on DNAPL migration in porous media: Insights from laboratory experiments and numerical modelling. Hydrogeol J 23 (8), 1703.
- [65] Zhou, A.-x, Zhang, Y.-l, Dong, T.-z, Lin, X.-y, Su, X.-s, 2015. Response of the microbial community to seasonal groundwater level fluctuations in petroleum hydrocarbon-contaminated groundwater. Environ Sci Pollut Res 22, 10094–10106. https://doi.org/10.1007/s11356-015-4183-6.